Journal of *Marine Science and Engineering*

MDPI

Article

Investigation into the Motion Characteristics and Impact Loads of Buoy Water Entry Under the Influence of Combined Waves and Currents

Wei Ge [1], Xiaolong Ying [2], Hailong Chen [2,*], Sheng Wu [2], Jian Zhang [3], Lixue Jiang [3] and Hengxu Liu [2]

[1] School of Mechanical Engineering, Shanghai Jiao Tong University, Shanghai 200240, China; 17317190246@163.com
[2] Yantai Research Institute, Harbin Engineering University, Yantai 265500, China; liuhengxu@hrbeu.edu.cn (H.L.)
[3] China Resources Gas Investment (China) Limited, Hong Kong 999077, China
* Correspondence: chenhailong@hrbeu.edu.cn

Abstract: As a crucial component in marine monitoring, meteorological observation, and navigation systems, studying the motion characteristics and impact loads of buoy water entry is vital for their long-term stability and reliability. When deployed, buoys undergo a complex motion process, including the impact of entering the water and a stable floating stage. During the water entry impact phase, the motion characteristics and impact loads involve interactions between the buoy and the water, the trajectory of motion, and dynamic water pressure, among other factors. In this paper, the VOF model is used to calculate the buoy's water entry motion characteristics, and then the STAR-CCM+&ABAQUS bidirectional fluid–structure interaction (FSI) method is used to calculate the water entry impact load of the buoy under different water surface conditions and different initial throwing conditions, considering the influence of the flow field on the structure and the influence of the structure deformation on the flow field. The study finds that under the influence of wave and current impacts, changes in wave height significantly affect the buoy's heave motions. Under different parametric conditions, due to the specific direction of wave and current impacts, the buoy's pitch amplitude is relatively more intense compared to its roll amplitude, yet both pitch and roll motions exhibit periodic patterns. The buoy's pitch motion is sensitive to changes in the entry angle; even small changes in this angle result in significant differences in pitch motion. Additionally, the entry angle significantly impacts the peak vertical overload on the buoy. Instantaneous stress increases sharply at the moment of water entry, particularly at the joints between the crossplate and the upper and lower panels, and where the mast connects to the upper panel, creating peak stress concentrations. In these concentrated stress areas, as the entry speed and angle increase, the maximum equivalent stress peak at the monitoring points rises significantly.

Keywords: buoy; the motion characteristics; impact loads of buoy water entry; VOF model; STAR-CCM+&ABAQUS bidirectional fluid–structure interaction (FSI) method

check for updates

Academic Editor: Giuseppe Giorgi

Received: 17 December 2024
Revised: 15 January 2025
Accepted: 20 January 2025
Published: 24 January 2025

Citation: Ge, W.; Ying, X.; Chen, H.; Wu, S.; Zhang, J.; Jiang, L.; Liu, H. Investigation into the Motion Characteristics and Impact Loads of Buoy Water Entry Under the Influence of Combined Waves and Currents. *J. Mar. Sci. Eng.* **2025**, *13*, 218. https://doi.org/10.3390/jmse13020218

Copyright: © 2025 by the authors. Licensee MDPI, Basel, Switzerland. This article is an open access article distributed under the terms and conditions of the Creative Commons Attribution (CC BY) license (https://creativecommons.org/licenses/by/4.0/).

1. Introduction

Ocean buoys, as important tools for ocean research and monitoring, are widely used in fields such as meteorology, marine environment, and ocean climate change. They can collect real-time ocean data, such as seawater temperature, salinity, wave height, and atmospheric pressure, providing support for scientific research, weather forecasting, and disaster early warning [1]. By deploying buoys, scientists can gain a deeper understanding of ocean

dynamics and reveal the interaction between the ocean and atmosphere, which is essential for the study of climate change, marine ecology, and other topics [2]. However, during the deployment of ocean buoys in deep-sea areas, factors such as large waves and ocean currents can cause severe collisions between the buoy and the water surface, potentially subjecting its precision sensors and overall structure to significant impact. During the impact, sensors undergo intense motion and vibrations, which may lead to damage to the sensors themselves and may affect the accuracy and reliability of data collection. Furthermore, the instantaneous structural stress generated during the buoy's water entry may also cause potential damage to its shell and internal components, thus affecting its long-term stability and performance. Therefore, studying the dynamic characteristics and impact load during the water entry process of ocean buoys is of vital practical significance for improving buoy design reliability, optimizing buoy structures, and extending their service life.

The core of the research on the dynamic characteristics and impact loads during the water entry process of ocean buoys lies in the water entry impact problem. Currently, scholars from various countries have conducted extensive and in-depth research on this issue. The theoretical research on water entry impact dates back to around the 1930s when Von Karman studied the landing of seaplanes and simplified the buoyant body to a wedge shape, deriving an impact formula using an asymptotic theory that agreed with the experimental results [3]. Building upon Von Karman's research, Wagner incorporated the variation of the free surface into the influencing factors and obtained detailed results for impact pressure and velocity fields using an improved asymptotic theory [4]. Dobrovol Skaya [5], Greenhow [6], and Zhao et al. [7,8] further investigated the impact of ideal incompressible liquids on structural bodies. Korobkin assumed water to be a compressible fluid and developed a theory for the impact of structural bodies on compressible fluids [9]. Fraenkel et al. theoretically analyzed the flow field changes caused by the vertical water entry of a wedge-shaped object at a fixed velocity [10]. Y. M. Scolan et al. proposed a more advanced inverse Wagner theory to analyze the water entry impact of three-dimensional blunt bodies, using the energy distribution method to correctly predict pressure distribution and dynamic pressures along the surface of the body [11].

With the widespread application of numerical simulation techniques to the hydrodynamic problems of offshore structures [12,13], researchers from various countries have also applied these techniques to the study of water entry impact. Wu et al. used FLUENT6.3 software to study the high-speed water entry of vehicles, gaining a deeper understanding of how attitude angle affects the flow field [14]. Qi et al. employed CFD methods to examine the water entry of air-dropped autonomous underwater vehicles (AUVs), preliminarily determining the relationship between impact load, vehicle speed, and angle [15]. Wang et al. simulated the water entry of vehicles with asymmetric head shapes using the volume of fluid (VOF) multiphase flow model [16]. Hu et al. used VOF to study the effect of different water entry speeds on the maximum pressure during the water entry of flat-bottomed structures in waves [17]. Takami et al. combined CFD and FEA to develop a numerical simulation method for calculating the overall and local impact pressures on ship structures under different impact loads and wave conditions. They compared the calculation results with other methods and experimental data, validating the effectiveness of their method [18]. Li et al. used CFD methods to investigate the effect of waves on the water entry of projectiles equipped with cavitators, thoroughly exploring the influence of wave height, entry angle, and speed on the water entry process and the potential mechanisms involved [19]. Zhang et al. conducted a numerical study on the inclined water entry of cylinders under different regular waves, analyzing the cavity evolution mechanism, dynamic characteristics,

and vortex structures [20]. Tregde et al. [21–25] used the finite volume method (FVM) to study the dynamic characteristics and impact pressures during the water entry of lifeboats.

In addition to using CFD technology to study water entry impact, scholars from various countries have also carried out experimental research. Breton et al. used LED edge illumination technology to experimentally study the vertical water entry of wedge-shaped objects and hemispheres, analyzing the evolution of wet surface areas under different conditions and comparing their experimental observations with theoretical predictions [26]. Some other studies include Wei and Hu [27], De Backer et al. [28], and Shams [29], who, respectively, studied the water entry of cylinders, cones, and wedges. Sun [30] and Yan [31] extensively studied cavity and jet evolution during the water entry of autonomous underwater vehicles (AUVs), cylinders, and projectiles with different nose shapes. Truscott [32] studied the water entry of rotating spheres, while Hurd et al. [33] investigated the water entry of deformable spheres. Li et al. [34] examined the water entry of spheres with different surface wettabilities, and Panciroli et al. [35] studied the dynamics of flexible cylindrical shells at the water surface. Ren et al. [36] researched the vertical water entry of flexible wedges into still water. Gilbarg and Anderson [37] studied the effects of impact velocity, atmospheric pressure, and density on the evolution of small spherical water entry cavities. May et al. [38,39] conducted extensive water entry experiments on axisymmetric structures (such as disks, cones, cylinders, and spheres), obtaining critical speeds for cavity formation, cavity development laws, fluid dynamics during water entry, and water entry ballistics and drag coefficients. Aristoff and Bush experimentally investigated the cavity characteristics of hydrophobic surface spheres [40]. Panciroli et al. conducted experiments on the water entry of flexible cylindrical bodies, varying the release height to alter water entry speed, and measured instantaneous deformations at specific surface features of the flexible cylinders [41]. Guo et al. [42,43] studied the high-speed horizontal water entry behavior of projectiles with different nose shapes through experiments and theoretical research, proposing a drag coefficient model independent of the cavitation number. Shi et al. experimentally studied the high-speed water entry of projectiles at 342 m/s, using non-intrusive optical measurement techniques to investigate the formation and collapse of super-cavitation [44]. Truscott et al. experimentally studied the fluid dynamics of spherical water entry at low Froude numbers by dropping a rotating sphere onto a horizontal free surface, investigating the effects of spin rate and impact velocity [45].

Current theoretical research, such as the inverse Wagner theory and compressible fluid theory, provides extensive analyses of water entry impacts for objects of various shapes, offering deep insights into the interactions between water and objects. However, some models still rely on simplifying assumptions and fail to fully capture the complexity of the actual water entry process. Currently, computational fluid dynamics (CFD) offers researchers a tool to gain a deeper understanding of the impacts of water entry, especially under the influence of complex factors like waves, speed, and angles, enabling the prediction of pressure variations and flow field evolution during the entry process. Nevertheless, CFD still has certain limitations, such as treating structures as rigid bodies and neglecting the effects of structural deformations on the flow field. Current research in the field of water entry impact primarily focuses on the following areas: In terms of research outcomes, the emphasis is on the water entry dynamic characteristics, structural response, etc., while the main research methods involve numerical simulation techniques and experimental methods. Most of the research focuses on the high-speed water entry of structures into still water, with less attention given to the study of low-speed water entry into non-stationary water surfaces. Therefore, this paper conducts a numerical simulation study on the low-speed water entry impact of ocean buoys under wave and current conditions, not only to enrich the research content in this field but also to assist researchers in predicting the

dynamic response of ocean buoys during water entry and formulating reasonable design parameters and deployment schemes.

2. Numerical Methods

This paper initially employs the overlapping grid method in STAR-CCM+ to calculate changes in the liquid surface, using the Reynolds-averaged Navier–Stokes (RANS) approach and the SST k-ε turbulence model to simulate the flow field changes, aimed at studying the water entry motion characteristics of buoys. Subsequently, a bidirectional fluid–structure interaction (FSI) computational method is established on the STAR-CCM+ and ABAQUS platforms to study the impact loads during buoy water entry. In the numerical simulation process, the fluid solver builds on the aforementioned theories, utilizing morphing mesh deformation technology to capture the movement and deformation information of the solid mesh. The solid solver uses solid elements to simulate the stress state and deformation of the solid, employing implicit dynamic time steps and a six-degrees-of-freedom-body model to simulate the motion process of the buoy structure. The fluid–structure interaction is bidirectional, allowing multiple exchanges and iterations of information between the solid and fluid solvers within a coupled time step, establishing a numerical computation method for fluid–structure interaction during the buoy water entry process.

2.1. Fluid Control Equations

STAR-CCM+2306 software discretizes the fluid governing equations using the finite volume method (FVM). The computational domain is subdivided into a finite number of adjacent control volumes, which can be polyhedral in shape. The fluid governing equations include the continuity equation and the momentum conservation equation. The solution process begins with solving the continuity and momentum conservation equations.

Continuity equation:

$$\frac{D\rho}{Dt} + \rho\nabla\cdot\boldsymbol{v} = 0 \tag{1}$$

where $\frac{D\rho}{Dt}$ represents the rate of change in the fluid's density with respect to time. For an incompressible fluid with viscosity, when $\frac{D\rho}{Dt} = 0$, Equation (1) simplifies to:

$$\frac{\partial u}{\partial x} + \frac{\partial v}{\partial y} + \frac{\partial w}{\partial z} = 0 \tag{2}$$

where u, v, and w are the velocity components of a fluid element in the x, y, and z directions.

The momentum equation (the Navier–Stokes equation), for a constant viscosity, is given by:

$$\begin{aligned}
\frac{Dv_x}{Dt} &= f_x - \frac{1}{\rho}\frac{\partial p}{\partial x} + \nu\left(\frac{\partial^2 v_x}{\partial x^2} + \frac{\partial^2 v_x}{\partial y^2} + \frac{\partial^2 v_x}{\partial z^2}\right) + \frac{1}{3}\nu\frac{\partial\nabla v}{\partial x} \\
\frac{Dv_y}{Dt} &= f_y - \frac{1}{\rho}\frac{\partial p}{\partial y} + \nu\left(\frac{\partial^2 v_y}{\partial x^2} + \frac{\partial^2 v_y}{\partial y^2} + \frac{\partial^2 v_y}{\partial z^2}\right) + \frac{1}{3}\nu\frac{\partial\nabla v}{\partial y} \\
\frac{Dv_z}{Dt} &= f_z - \frac{1}{\rho}\frac{\partial p}{\partial z} + \nu\left(\frac{\partial^2 v_z}{\partial x^2} + \frac{\partial^2 v_z}{\partial y^2} + \frac{\partial^2 v_z}{\partial z^2}\right) + \frac{1}{3}\nu\frac{\partial\nabla v}{\partial z}
\end{aligned} \tag{3}$$

In vector form, this becomes:

$$\frac{D\boldsymbol{v}}{Dt} = \boldsymbol{f} - \frac{1}{\rho}\nabla p + \nu\nabla^2\boldsymbol{v} + \frac{1}{3}\nu\nabla(\nabla\cdot\boldsymbol{v}) \tag{4}$$

For incompressible fluids with a constant viscosity, the Navier–Stokes equation simplifies to:

$$\frac{\partial\boldsymbol{v}}{\partial t} + (\boldsymbol{v}\cdot\nabla)\boldsymbol{v} = \boldsymbol{f} - \frac{1}{\rho}\nabla p + \nu\nabla^2\boldsymbol{v} \tag{5}$$

where the terms from left to right represent: the unsteady term, the convective term, the body force per unit mass, the pressure gradient term per unit mass, and the diffusion or viscous force term.

2.2. Structural Calculation Equations

In the bidirectional fluid–structure interaction method, the structural equations include the rigid body motion and the deformation of the structure. Initially ignoring the structure's deformation, it is assumed that the structure undergoes six-degrees-of-freedom motion during water entry, treating the structure as a rigid body. According to classical mechanics, rigid body motion includes three linear momentum equations and three angular momentum equations, totaling six motion control equations.

Linear momentum equation:

$$\frac{d(mu_c)}{dt} = F \tag{6}$$

Angular momentum equation:

$$\frac{d(I_c \cdot w)}{dt} = M_c \tag{7}$$

In the structural mass m, u_c represents the velocity of the structure's center of mass, I_c is the structure's moment of inertia, and w is the angular velocity of the structure. F and M_c represent the forces and torques acting on the structure, respectively. The forces on the structure are primarily composed of fluid loads due to shear stresses and body forces caused by pressure distributions.

In terms of structural dynamic response, ABAQUS discretizes the three-dimensional elastic dynamic equations of the structural finite element model to obtain information on the structure's deformation, stress, and strain.

Structural dynamics equation:

$$\begin{cases} \sigma_{ij,j} + f_i - \rho s_{i,tt} - \mu s_{i,t} = 0 \\ \varepsilon_{ij} = \frac{1}{2}(s_{i,j} + s_{j,i}) \\ \sigma_{ij} = D_{ijkl}\varepsilon_{kl} \end{cases} \tag{8}$$

where ρ is the density, μ represents the damping coefficient, $s_{i,t}$ and $s_{i,tt}$ are the first and second time derivatives of displacement, representing the velocity and acceleration in the i direction, $\sigma_{ij,j}$ represents the divergence of the stress tensor, indicating the rate of change in stress in a particular direction, f_i represents the force per unit volume (e.g., gravity or other external force), ε_{ij} represents the component of the strain tensor, $s_{i,j}$ represents the derivative of the displacement component with respect to spatial coordinates (representing the change in displacement in space), and $s_{j,i}$ represents the inverse spatial derivative of the displacement component. σ_{ij} represents the components of the stress tensor, where i and j are component indexes of the stress; D_{ijkl} represents the constitutive tensor of the material, usually related to elastic modulus or stiffness, defining the relationship between stress and strain; and ε_{kl} represents the strain component.

After constructing shape functions for the above equations and the corresponding boundary conditions, equivalent integration can be performed to obtain:

$$\int_{\mathrm{v}} \left(\delta\varepsilon_{ij} D_{ijkl}\varepsilon_{kl} + \delta s_i \rho s_{i,t} + \delta s_i \mu s_{i,t}\right) \mathrm{dV} = \int_{\mathrm{v}} \delta s_i f_i \mathrm{dV} + \int_S \delta s_i \sigma_{ij} n_j \mathrm{d}S \tag{9}$$

The final discretized equations for system solution:

$$\mathbf{M}\ddot{\mathbf{a}}(t) + \mathbf{C}\dot{\mathbf{a}}(t) + \mathbf{K}\mathbf{a}(t) = \mathbf{Q}(t) \tag{10}$$

where $\dot{\mathbf{a}}(t)$ and $\ddot{\mathbf{a}}(t)$ represent the nodal velocity and acceleration vectors, $\mathbf{M}$ is the mass matrix, $\mathbf{C}$ is the damping matrix, $\mathbf{K}$ is the stiffness matrix, and $\mathbf{Q}(t)$ represents the load vector, which consists of the element matrices and element load vectors.

$$\mathbf{M} = \sum_e \mathbf{M}_e \quad \mathbf{C} = \sum_e \mathbf{C}_e \tag{11}$$

$$\mathbf{K} = \sum_e \mathbf{K}_e \quad \mathbf{Q} = \sum_e \mathbf{Q}_e \tag{12}$$

In ABAQUS, the central difference method and the HHT (Hilber–Hughes–Taylor) time integration method are available for solving the dynamic equations set (8). The central difference method is an explicit time integration technique, often used for solving nonlinear dynamic problems. The HHT method is an implicit time integration technique that uses displacement vectors from adjacent time points to represent the dynamics equation's $\dot{\mathbf{a}}(t)$ and $\ddot{\mathbf{a}}(t)$ vectors, solving iteratively. Considering the need for multiple exchanges of fluid–structure interaction information and computational stability, this paper employs the HHT time integration method to solve the structural equations.

2.3. VOF Model

The volume of fluid (VOF) model is a simplified multiphase model suitable for simulating the flows of several immiscible fluids on numerical grids, and is capable of resolving interfaces between various phases. For the air–liquid two-phase flow problem, the volume fraction of the liquid phase is α_l and the volume fraction of the air phase is $\alpha_a = 1 - \alpha_l$.

$\alpha_l = 0$ and $\alpha_l = 1$ indicate that the cell is completely void in phase liquid and filled in phase air, respectively. $0 \leq \alpha_l \leq 1$ shows the values between the two limits, which indicates the presence of an interface between the phases. An example of $\alpha_l = 0.5$ can represent the liquid–liquid free surface. The material properties of the phases that are calculated in the cells containing the interfaces of constituent fluids. The fluids that are presented in the containing cells of the same interface are treated as a mixture as follows:

$$\rho = \rho_l \alpha_l + \rho_a \tag{13}$$

$$\mu = \mu_l \alpha_l + \mu_a \alpha_a \tag{14}$$

where ρ_l and ρ_a are the densities and μ_l and μ_a are the dynamic viscosities of the liquid and air phases, respectively.

2.4. Numerical Method Computational Domain Conditions and Mesh Setup

2.4.1. CFD Computational Domain Conditions and Mesh Setup

Figure 1 shows a schematic diagram of the mesh scenario for a cylindrical buoy entering the water at an angle $\theta_{initial}$, at a distance $h_{initial}$ from the water surface, impacting the wave surface with an initial velocity v_v (the resultant velocity in the direction of the buoy's movement, with velocity components v_x, v_y, v_z). The inertial frame O−XYZ is fixed in the inertial space and an appropriate location on the water surface is selected for the origin O. In the local coordinate system *o-xyz*, the origin o is set at the center of the circle at the bottom of the buoy, and the direction of the *z* axis coincides with the symmetry axis of the buoy.

The buoy model is derived from a widely used medium-sized integrated marine observation buoy, simplified to form a structural model. The scale of the model is 1:1 in comparison to the physical model. Both the buoy model and the physical model are made of polyethylene material, with a wall thickness of 0.05 m, a total height of 2.15 m, and a weight of 907 kg. The center of mass is located at the coordinates (0, 0, 1.257). The specific dimensional parameters are shown in Figure 2, with D = 2 m.

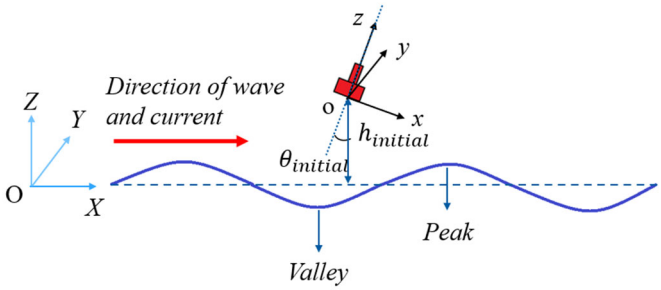


Figure 1. Schematic of the original physical scenario of a cylindrical buoy entering water at an angle.

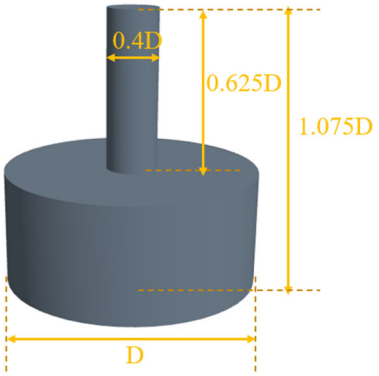


Figure 2. Cylindrical buoy geometric model and its dimensional parameters.

In the study of the buoy's water entry impact motion characteristics, factors such as wave height, entry speed, and entry angle are considered for their effects on the impact motion characteristics of the buoy, with a focus on analyzing physical parameters critical to the buoy's safe and stable operation such as heave, surge, roll, pitch, and acceleration. Table 1 displays the operational parameter values for the buoy's water entry.

Table 1. Parameter values for buoy model water entry impact conditions.

Parametric Study Name	Buoy Head	h (m)	v_f (m/s)	v_v (m/s)	$\theta_{initial}$ (Degree)
Wave height	Cylinder	0.5 1 2	1	$v_x = -1.82$ m/s $v_y = 0$ m/s $v_z = -5$ m/s	20°
Initial entry angle	Cylinder	2	1	$v_v = 5$ m/s	0° 10° 20°
Initial entry velocity	Cylinder	2	1	$v_z = 0$ m/s $v_z = -5$ m/s $v_z = -10$ m/s	0°

Based on wave theory and integrating the VOF (volume of fluid) technique for tracking the fluid–solid interface, this paper employs the boundary condition wave-making method (velocity inlet wave-making) from numerical wave-making techniques. Utilizing first-order Stokes wave theory, a velocity formula is derived, establishing a given boundary velocity distribution to achieve three-dimensional numerical wave-making.

The wave-making domain in the numerical wave tank spans 100D in length, with a wave damping zone measuring 50D. As shown in Figure 3, the numerical wave tank is sized at 150D × 12.5D × 15D and is divided using a hexahedral structured mesh. The boundary settings for the computational domain of the numerical wave tank are as follows:

the left side boundary, and the top boundary are set as velocity inlets; the bottom boundary, and the right side boundary is a pressure outlet; the front and back sides are symmetry planes. The entire domain is divided into three zones: the wave-generating zone, the working zone, and the wave-absorbing zone.

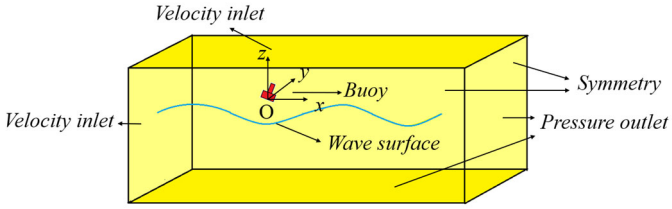


Figure 3. Computational domain boundary types.

Figure 4 shows the mesh grid of the computational domain. The mesh utilizes the computationally efficient Trimmer mesh, with densification around the buoy area and its movement to achieve more accurate simulation results. The size of the moving region is 10D × 10D × 12.5D, and the diameter of the overlapping mesh area is 1.4D. The base grid size of the computational domain is 2 m, with a grid size of 0.7 m at the water surface. The grid size in the x and y directions at the water surface is 0.6 m, and in the z direction, it is 0.05 m. The grid base size in the motion area is 0.7 m, and the grid size on the model surface is 0.1 m.

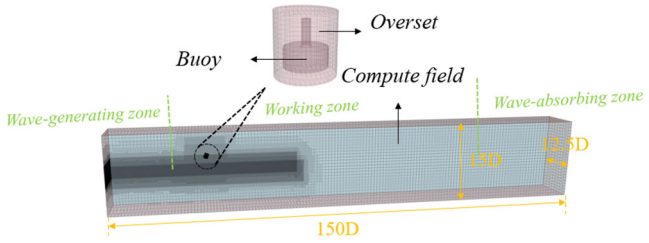


Figure 4. Computational domain mesh.

In this study, simulations were conducted using the computational fluid dynamics (CFD) software STAR-CCM+. The volume of fluid (VOF) model was employed to simulate multiphase fluid dynamics on a numerical grid, using first-order VOF waves to model the wave surface. A six-degrees-of-freedom rigid body was modeled for the buoy using the overlapping mesh combined with the DFBI model, calculating the fluid forces, fluid torque, and gravity acting on the rigid body. By modeling the surface tension in the fluid, free surface flow was achieved, ensuring the stability of the fluid dynamics and more realistically simulating the water–air interface area. The control equations were discretized using the finite volume method. The time step chosen for this study was 5×10^{-3} s to ensure that the Courant number remained below 1, thus achieving stability during the computations; the simulation duration is 10 s.

2.4.2. CAE and CFD Fluid–Structure Interaction Computational Domain, Mesh Setup, and Monitoring Points Setup

In the study of water entry impact loads on buoys, a bidirectional fluid–structure interaction (FSI) method using CAE and CFD was employed, focusing on the cylindrical buoy model and its previously mentioned coordinate system. The computational domain mesh was refined twice for both the buoy and the wave surface, with an overlapping mesh diameter of 7 m. This study emphasizes the effects of wave height, entry angle, and entry speed on the impact loads on both the external and internal structures of the buoy, with specific operational parameter values as previously listed in Table 1.

As shown in Figures 5 and 6, the mesh setup for the CFD computational domain in the joint CAE and CFD simulation is essentially the same as that used for calculating the buoy's water entry motion characteristics. During the refinement of the buoy motion model, a dual-layer mesh refinement was employed. In the joint CAE and CFD simulation, the DFBI motion was moved to CAE software (ABAQUS2022) for predefined field settings, and structural elements were assigned gravitational fields within CAE; Table 2 shows the material properties of the PE material used for the buoy. In the CAE model setup for the buoy, the density, elastic modulus, and Poisson's ratio are specified.

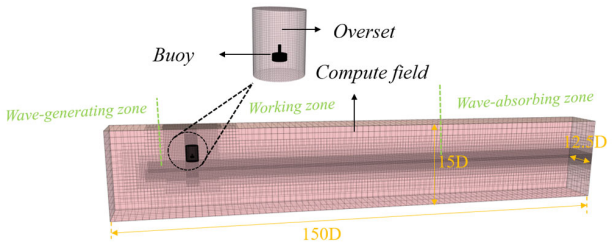


Figure 5. CFD computational domain mesh in co-simulation.

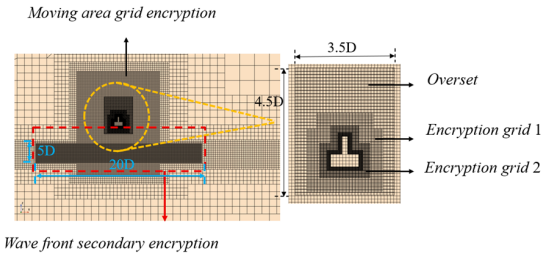


Figure 6. Refined area mesh division.

Table 2. Material properties.

Properties	Parameters
Density ρ	910 kg/m^3
Elastic Modulus E	0.85 GPa
Poisson's Ratio μ	0.35
Yield Strength R	25 MPa

Figure 7 shows a comparison of the mesh division for the CFD buoy model and the CAE buoy model. In CAE, the cylindrical buoy is meshed using hexahedral elements, with mesh sizes controlled within the range of 0.0025D to 0.01D, consistent with the mesh size range of the CFD buoy model.

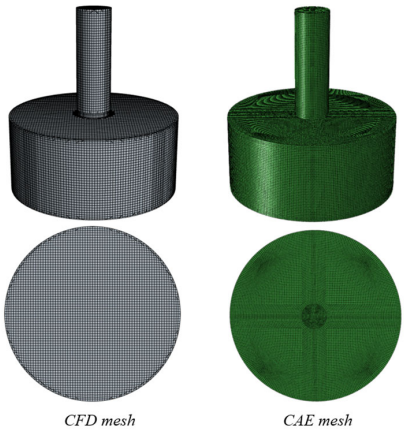
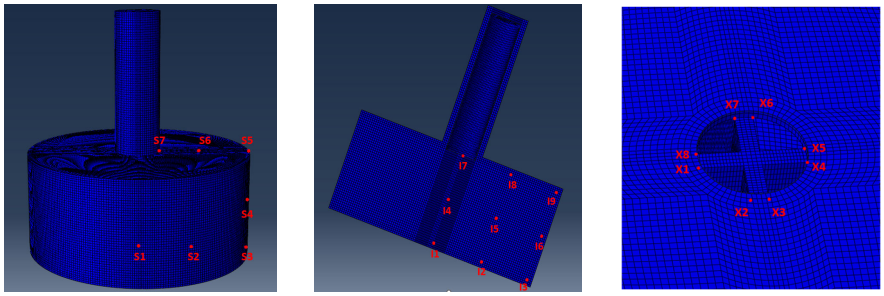


Figure 7. Mesh division of CFD buoy model and CAE buoy model.

In the study of the water entry impact load characteristics of buoys, the computational fluid dynamics (CFD) software STAR-CCM+ and the finite element software (CAE) ABAQUS are used for bidirectional fluid–structure interaction research. The fluid–structure interaction process is bidirectional; the flow of the fluid affects the deformation of the solid structure, and the deformation of the solid, in turn, influences the flow of the fluid. This process facilitates multiple exchanges and iterations of information between the solid solver and the fluid solver within a single coupling time step, establishing a numerical computation method for fluid–structure interaction during the buoy's water entry. The time step in STAR-CCM+ is set to 1×10^{-3} s, while in ABAQUS, the initial time step is set to 1×10^{-3} s with a minimum increment step of 1×10^{-6} s, and the coupling method selected is implicit coupling.

As shown in Figure 8, monitoring points S1 to S7 are set up in the external area of the buoy, monitoring points I1 to I8 are placed on the internal reinforced crossplate surfaces, and monitoring points X1 to X8 are established at the junctions between the upper panel and the internal reinforced crossplates.



(**a**) (**b**) (**c**)

Figure 8. Layout of monitoring points. (**a**) External monitoring points S1 to S7; (**b**) internal reinforced crossplate surface monitoring points I1 to I9; (**c**) monitoring points X1 to X8 at the junction of the upper panel and internal reinforced crossplates.

2.5. CFD Mesh Convergence Verification and Waveform Validation

The grid division of the computing domain directly determines the accuracy of the numerical simulation. In this section, three sets of grids with different mesh densities are established, respectively, for numerical simulation of motion characteristics and impact load without changing the overall grid division law. The total number of grids is shown in Table 3. The time step for numerical simulation of motion characteristics is 5×10^{-3} s and the simulation time is 10 s. The time step for the impact load is 1×10^{-3} s and the simulation time is 3 s. Under the conditions of wave height h = 2 m, current velocity v_v = 1 m/s, and distance from the horizontal plane h = 5 m, the vertical entry process of the buoy with initial an entry velocity of $v_v = -10$ m/s and an initial entry angle of $\theta_{initial} = 0°$ was numerically simulated. The floating motion curves of the buoy under different mesh densities, as shown in Figure 9, and the maximum equivalent stress variation curves of the buoy's external monitoring points, as shown in Figure 10, were obtained. As can be seen from Figure 9, the difference between the sag calculation results of the three mesh densities is within 5%. After considering the calculation accuracy and time cost comprehensively, a mesh with 6.48 million mesh numbers was finally selected for numerical simulation of the motion characteristics. As can be seen from Figure 10, the difference between the calculated results of maximum equivalent stress at the external monitoring point S2 of the three mesh densities is within 8%. In the final numerical simulation of impact load, a grid with 2.68 million mesh numbers was selected for the calculation.

Table 3. Number of grids.

Number	Mesh Quality	Total Number of CFD Grids (1×10^4)	Total Number of CFD Grids in Co-Simulation (1×10^4)
I	Rough	500	203
II	Medium	648	268
III	Fine	720	355

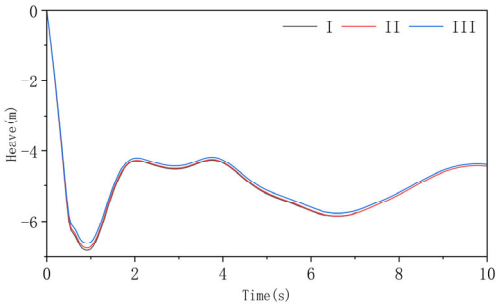


Figure 9. Heave data curves at different mesh densities.

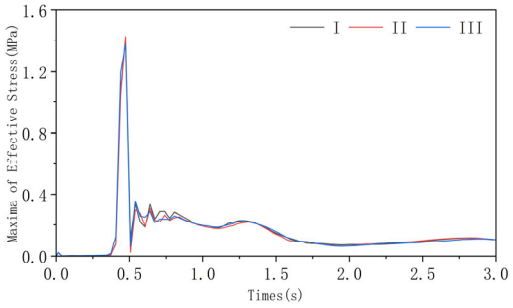


Figure 10. Impact load data curves at different mesh densities.

In order to eliminate the reflected wave on the boundary, the damped wave dissipation is set at the exit, the distance is 1.5~2 times the wavelength, and the specific setting value is 90 m. The simulated wave parameter information can be seen in Table 4. To accurately capture wave attenuation, three equidistant free surface wave height monitors were set up in the numerical wave tank, as shown in Figure 11; to monitor changes in wave shape over time within the computational domain, the distance between each pair of wave height gauges is 60 m, with L1 located 30 m from the left-side velocity inlet.

Table 4. Wave parameters used in testing.

Parameters	Values
Wave Height h (m)	2
Wave Length λ (m)	60
Period T (s)	5.8
Wave Speed v/(m·s^{-1})	10.34
Water Depth (m)	15

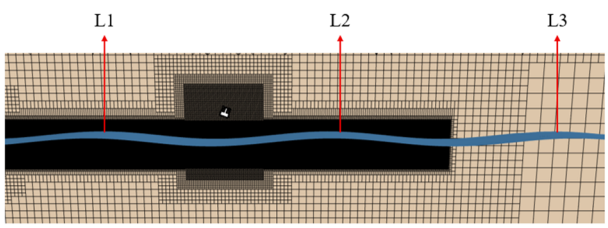


Figure 11. Wave height monitoring locations.

The wave amplitude over time at the wave height monitor locations is shown in Figure 12, with the numerical simulation producing an average wave height of 2.02 m.

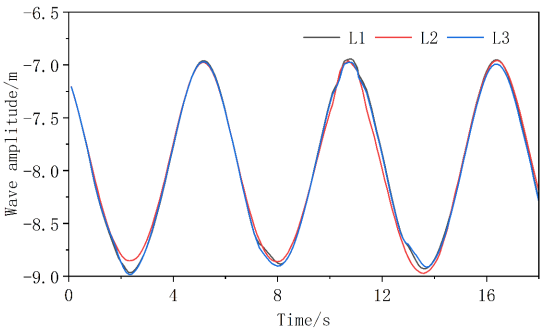


Figure 12. Results of wave height monitoring.

2.6. Validation of Numerical Methods

2.6.1. Validation of CFD Numerical Methods

Hou et al. [46] investigated the complex unsteady characteristics of a cylindrical body entering water from both numerical and experimental perspectives. In the numerical study, three-dimensional simulations with a six-degree-of-freedom model were conducted, in which the large eddy simulation (LES) and volume of fluid (VOF) techniques were applied for turbulence calculations and tracking the air–water interface, respectively. Corresponding experiments were also carried out, using a high-speed camera to record the evolution of the cavity. To verify the accuracy of the numerical methods, a solid aluminum cylinder model from the literature was used for validation. The model had a length of 200 mm, a diameter of 50 mm, and a weight of 1.06 kg. According to the initial parameters from the literature, the entry angle was 60° and the entry speed was 4.35 m/s. As shown in Figure 13, the angular data obtained from the numerical simulations in this study were compared with both the numerical simulation results and experimental results from the literature. The comparison reveals that the numerical results in this study have an error of less than 5% compared to the literature's numerical results, and an error of less than 9% compared to the experimental results. This demonstrates the reliability of the numerical simulation method presented in this study.

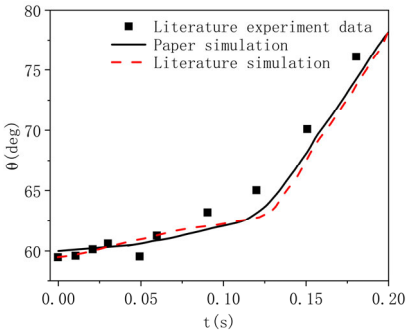


Figure 13. Comparison of pitch angle changes between this study's numerical simulation and literature/experimental data.

2.6.2. Validation of CAE and CFD Fluid–Structure Interaction Numerical Methods

Li et al. [47] designed a comprehensive experimental model and established a data acquisition system to capture the structural response of a rotating body during the entire oblique water impact process. In their study, strain gauges installed on the surface of the rotating body were used to measure the axial impact load and effective stress throughout the water entry impact process. To verify the accuracy of the numerical method, this study

adopted the rotating body model from the referenced literature for validation. The model has a maximum outer diameter of 200 mm, a total length of 390 mm, and a maximum weight of 4.273 kg. According to the initial parameters provided in the literature, with an entry angle of 30° and an entry speed of 6.16 m/s, the numerical simulations of the rotating body model were conducted. The effective stress at points S1 and S3 obtained from the numerical simulations were then compared with the literature experimental results from the referenced paper. Figure 14 provides a detailed description of the rotating body model and the setup of the effective stress monitoring points. As shown in Figure 15, the comparison between the numerical simulation results of the effective stresses at points S1 and S3 and the literature experimental results from the referenced paper shows an error within 8%, which ensures the reliability of the bidirectional fluid–structure interaction numerical method used in this study.

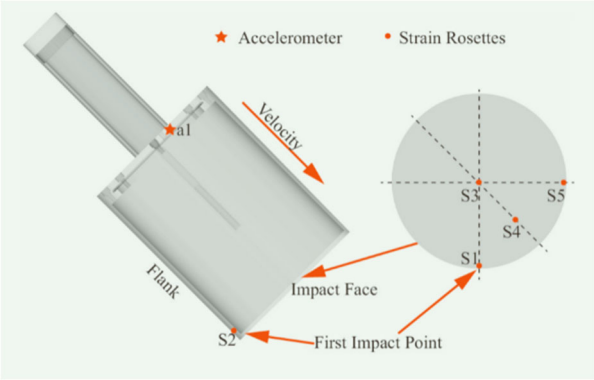


Figure 14. The structure of the rotating body model and the setup of monitoring points in the referenced literature.

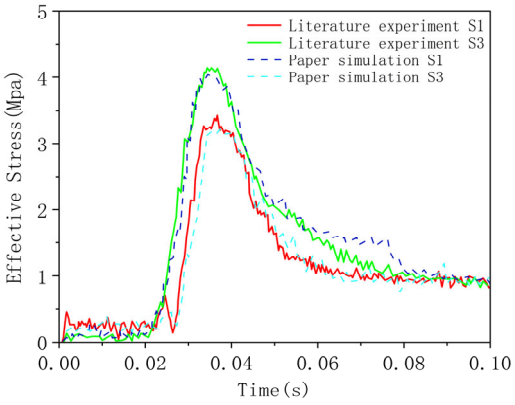


Figure 15. The comparison between the effective stress data of S1 and S3 obtained from the numerical simulation in this study and the experimental data from the referenced paper.

3. Results and Discussion

A cylindrical buoy drops from a height $h_{initial}$ = 5 m above the horizontal plane at speeds $v_x = -1.82$ m/s, $v_y = 0$ m/s, and $v_z = -5$ m/s, with a tilt angle $\theta_{initial} = 20°$, impacting the wave surface. The buoy's water entry motion characteristics and impact load properties are significantly influenced by wave dynamics. As shown in Figure 16, changes in the wave amplitude alter the relative motion distance between the buoy and the water surface, thus affecting its water entry depth and attitude upon entry. The impact loads on the buoy during water entry depend not only on the buoy's speed but are also closely related to the dynamic action of the waves. The wave surface generates varying intensities of hydrodynamic forces at the moment of water entry, leading to instantaneous increases

in impact loads, which typically manifest as short-duration peak values, impacting the structural safety of the buoy.

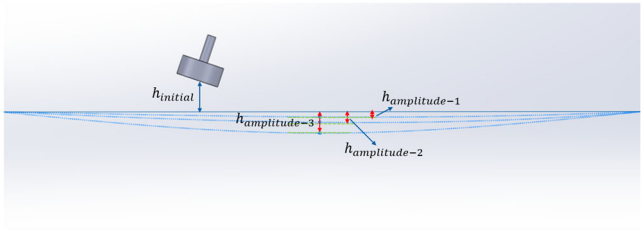
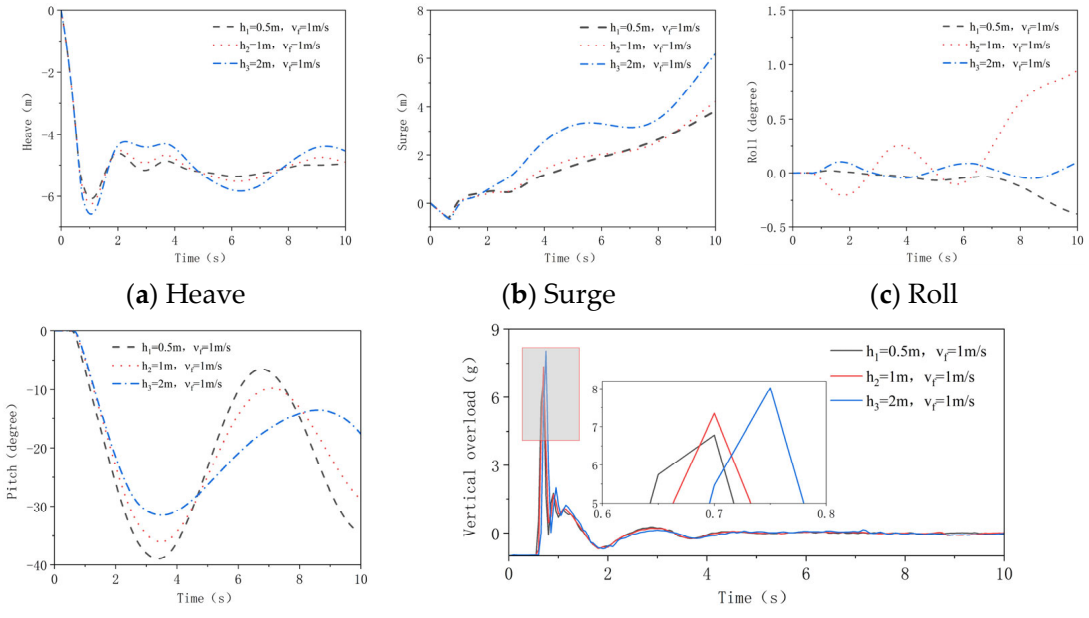


Figure 16. A schematic of the buoy's inclined water entry at different wave heights ($h_{amplitude}$ = h/2, $h_{amplitude-1}$ = 0.25 m, $h_{amplitude-2}$ = 0.5 m, $h_{amplitude-3}$ = 1 m).

3.1. The Impact of Parametric Conditions on the Buoy's Water Entry Motion Characteristics

3.1.1. Wave Height

By analyzing the heave motion data of the buoy after immersion under three different wave height conditions in Figure 17a, it was observed that the maximum immersion depth of the buoy increases with the wave height. As shown in Figure 18, this can be attributed to the fact that as the wave height increases, the vertical distance between the buoy's immersion position on the wave surface, and its initial position also increases, resulting in greater impact kinetic energy. Therefore, the buoy's maximum immersion depth increases, with the maximum depths reached being h_{max-1} = 6.07 m, h_{max-2} = 6.24 m, and h_{max-3} = 6.56 m, respectively. Subsequently, under the influence of buoyancy, the buoy moves upward. Within t = 4.6~10 s, under the combined effect of buoyancy and the buoy's inertia, the buoy exhibits periodic oscillatory motion across all wave heights. At a wave height of h_3 = 2 m, the buoy's heave motion amplitude is the largest. By analyzing the surge motion data of the buoy after immersion under three wave height conditions in Figure 17b, it was found that within t = 0~2 s, the surge motion variations of the buoy are nearly identical across all three wave heights, indicating that during this period, the influence of wave currents is minimal, and the buoy's inertial motion predominates in the longitudinal displacement.



(**a**) Heave (**b**) Surge (**c**) Roll

(**d**) Pitch (**e**) Vertical Overload

Figure 17. The motion characteristics of the buoy under different wave height conditions.

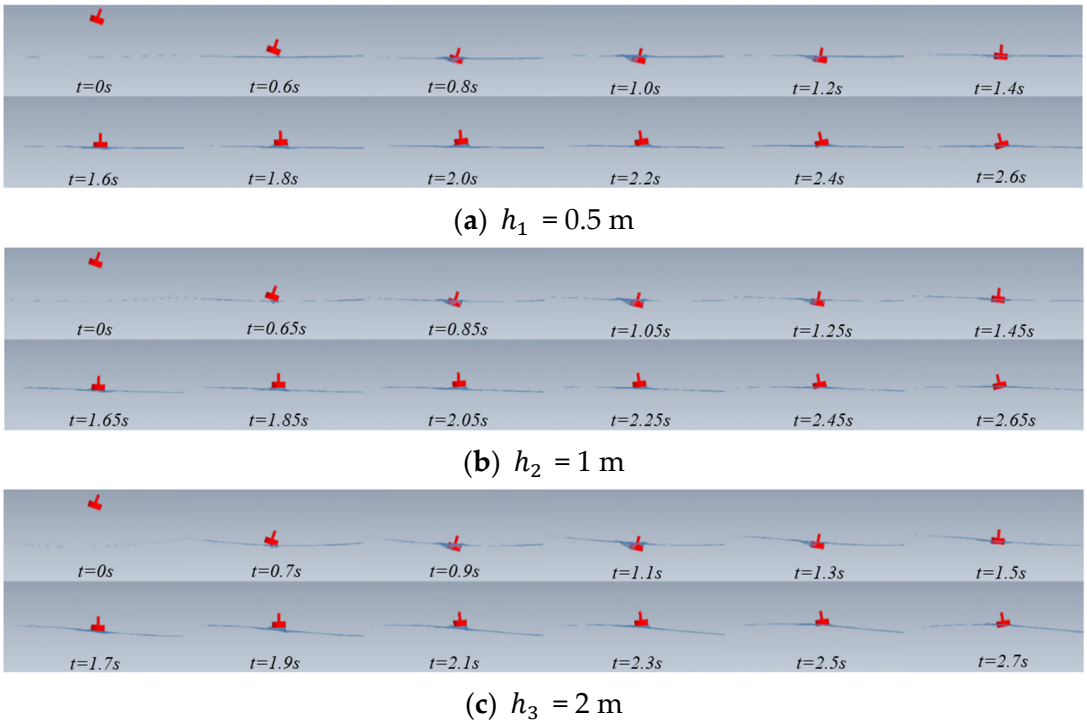


Figure 18. The motion attitude of the buoy under different wave height conditions.

The roll motion data of the buoy after immersion under three different wave height conditions, as shown in Figure 17c, were analyzed. Under the wave height condition of h_3 = 2 m, the buoy exhibits a clear periodic roll motion due to the periodic torque generated by wave currents around the buoy and the buoy's inertial response, with a period of T_{Roll} = 4.1 s and an amplitude of θ_{Roll} = 0.12°. Under the wave height conditions h_1 and h_2, the roll angle of the buoy gradually increases after t = 8 s. Comparing the roll motion data in Figure 17c with the pitch motion data in Figure 17d, it was observed that the variation in the roll angle is relatively small across all three wave heights, with θ_{Roll} being less than 1.3°. Further analysis of the pitch motion data in Figures 17d and 18 shows that the buoy's pitch motion exhibits periodic behavior under all three wave height conditions. As wave height increases, the pitch amplitude decreases. The pitch amplitudes corresponding to the three wave heights are $\theta_{Pitch-1}$ = 17.5°, $\theta_{Pitch-2}$ = 13.5°, and $\theta_{Pitch-3}$ = 9.5°, indicating that with higher wave heights, the buoy experiences increased longitudinal resistance. Specifically, the viscous force of water and buoyancy enhance the resistance against the buoy, causing the longitudinal motion of the buoy to gradually stabilize. Analysis of the vertical overload variations of the buoy after immersion under three wave height conditions, as shown in Figure 17e, reveals that at t = 0.7 s, the maximum vertical overloads of the buoy are a_{va-1} = 66.58 g (where g is the acceleration due to gravity) for h_1 = 0.5 m, and a_{va-2} = 72.12 g for h_2 = 1 m. For the wave height h_3 = 2 m, the maximum vertical overload is a_{va-3} = 78.74 g. Within t = 0~10 s, the variation in vertical overload gradually decreases under all three wave height conditions. This is because as wave height increases, the impact force of the waves increases, resulting in higher accelerations for the buoy. However, as time progresses, the dynamic interaction between the buoy and the wave surface stabilizes, causing the amplitude of the overload variations to decrease.

3.1.2. Entry Speed

As shown in Figure 19a, when the buoy impacts the wave surface vertically at speeds of v_v = 0 m/s, v_v = −5 m/s, and −10 m/s, it reaches its maximum water entry depth at t_1 = 1.45 s, t_2 = 1.1 s, and t_3 = 0.9 s, with maximum depths of h_{max-1} = 6.04 m,

h_{max-2} = 6.30 m, and h_{max-3} = 6.76 m, respectively. The greater the vertical speed of the buoy, the larger its initial momentum, thus the greater the vertical travel distance. From t = 6~10 s, the differences in heave motion corresponding to different entry speeds are relatively minor.

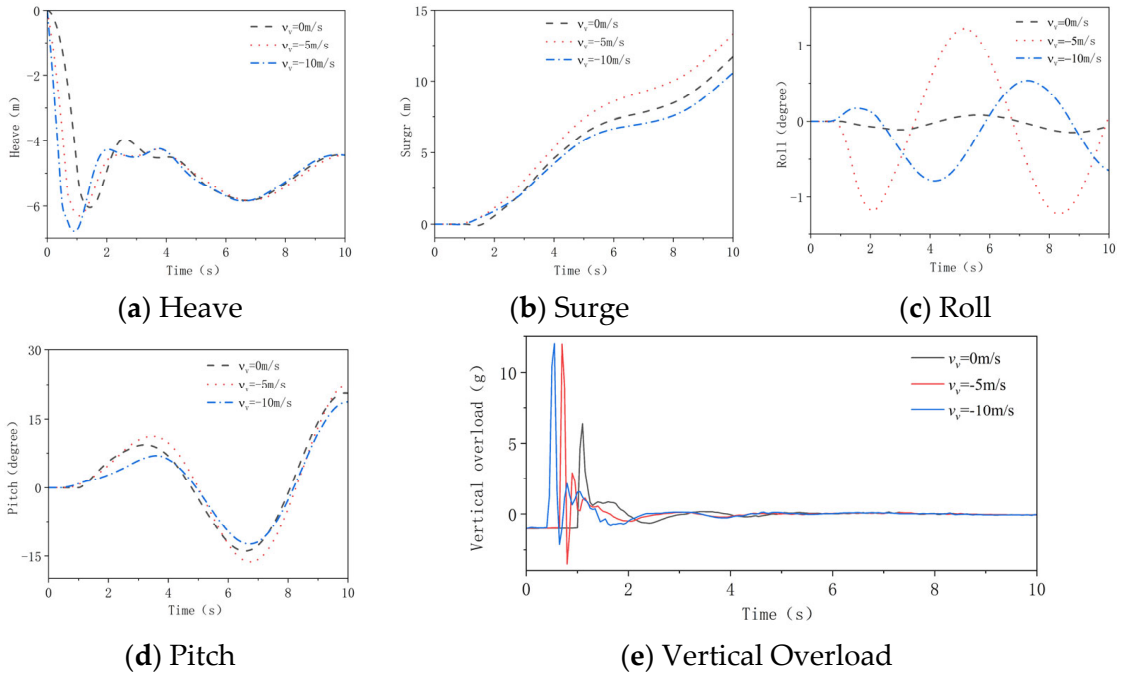
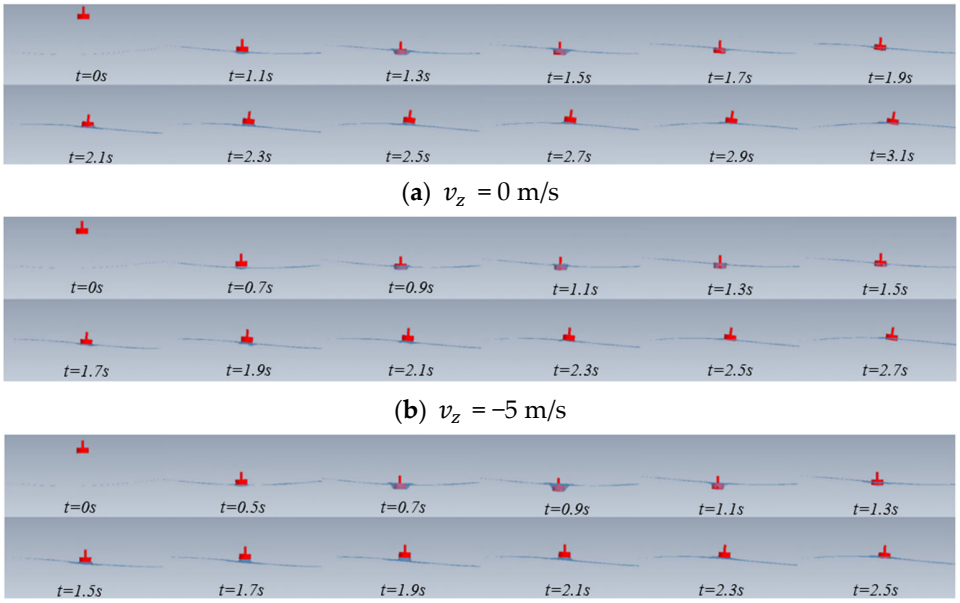


Figure 19. The motion characteristics of the buoy under different entry speed conditions.

In the buoy's longitudinal motion variation under three different entry velocities shown in Figure 19b, the changes in longitudinal motion at different velocities are similar. This similarity arises because the buoy is subjected to the same wave height and flow speed conditions, meaning the flow field environment is consistent. Consequently, the fluid resistance and the buoy's inertial response exhibit similar trends. As shown in Figure 20, the wave flow direction is along the positive x-axis, so the buoy is primarily influenced by the wave flow in the x-direction. The buoy experiences minimal lateral disturbances, resulting in a small roll motion amplitude, while the amplitude of the pitch motion along the y-axis is relatively larger. The roll motion amplitudes of the buoy under the three velocities are θ_{Roll-1} = 0.11°, θ_{Roll-2} = 1.18°, and θ_{Roll-3} = 0.17°, with minimal differences in pitch motion amplitude, indicating that the wave flow's influence on the pitch motion is relatively consistent. From the analysis of the vertical overload variations of the buoy after immersion under three different entry velocity conditions, as shown in Figure 19e, it can be seen that at t = 0.7 s, due to different initial entry velocities, the buoy contacts the wave surface at different times. The buoy reaches maximum vertical overload at t = 1.1 s, t = 0.75 s, and t = 0.55 s for the three velocities, with vertical overloads a_{va-1} = 62.73 g, a_{va-2} = 117.36 g, and a_{va-3} = 117.69 g, respectively. The higher entry velocities lead to shorter contact times with the wave surface, resulting in stronger reaction forces from the water, causing larger vertical overloads. Within t = 6~10 s, after the buoy enters the wave surface, the water's resistance gradually increases, reducing its acceleration. Therefore, the vertical overload of the buoy tends toward zero under all three entry velocity conditions.



(**a**) v_z = 0 m/s

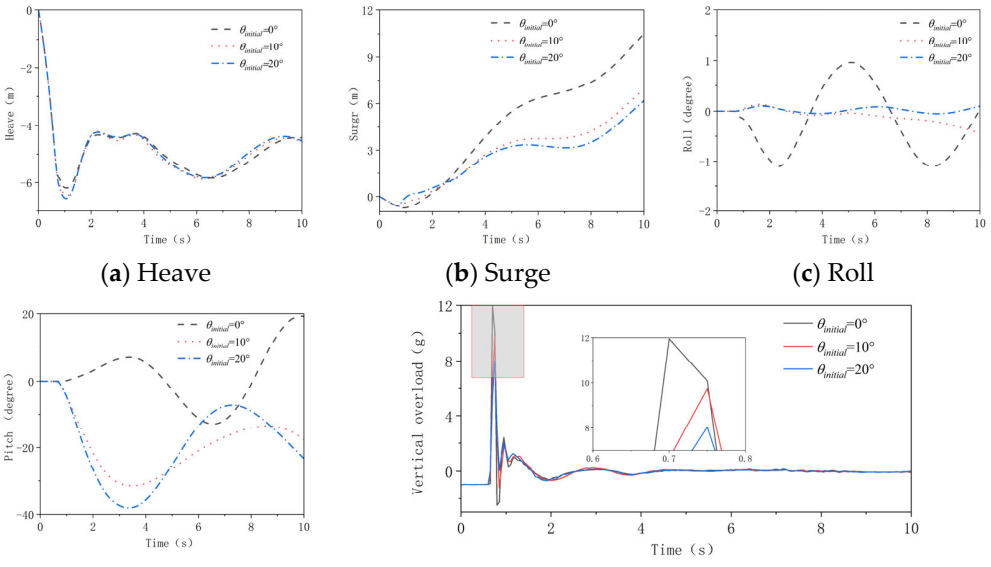
(**b**) v_z = −5 m/s

(**c**) v_z = −10 m/s

Figure 20. The motion attitude of the buoy under different entry speed conditions.

3.1.3. Entry Angle

As shown in Figure 21, when the buoy structure enters the water at different angles with the same velocity in the same direction of motion, the variation in vertical displacement is relatively small across the three entry angles under identical wave height conditions. In the vertical motion variation of the buoy structure for the three entry angles, when the buoy enters at 0°, 10°, and 20°, the maximum immersion depths are reached at t = 1.05 s, t = 1.1 s, and t = 1.05 s, with maximum immersion depths of h_{max-1} = 6.19 m, h_{max-2} = 6.46 m, and h_{max-3} = 6.56 m, respectively. This is because the vertical motion of the buoy on the wave surface is primarily influenced by the wave amplitude, the buoy's geometry, and fluid resistance. When the wave height and flow velocity remain consistent, the geometric shape of the buoy and the wave characteristics have a relatively balanced effect across different entry angles.

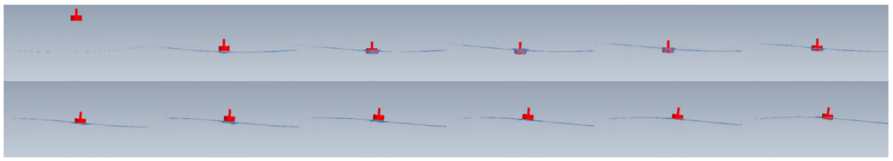


(**a**) Heave (**b**) Surge (**c**) Roll

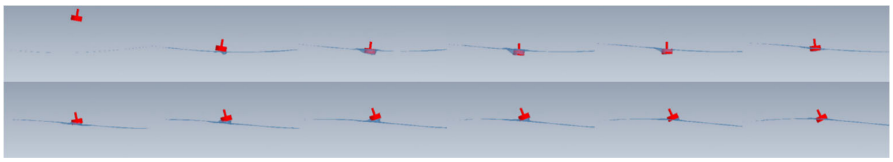
(**d**) Pitch (**e**) Vertical Overload

Figure 21. The motion characteristics of the buoy under different entry angle conditions.

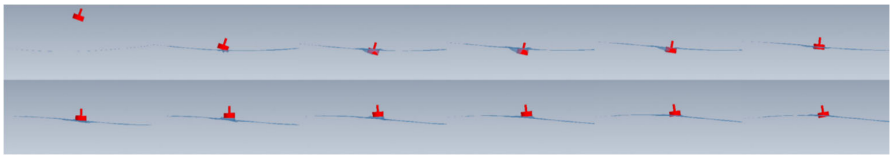
As shown in Figure 21b, in the surge motion variation diagrams of the buoy structure at three different entry angles, the surge displacement decreases with an increase in the buoy's entry angle. At t = 10 s, the surge displacements are $x_{Surge-1}$ = 10.59 m, $x_{Surge-2}$ = 6.92 m, and $x_{Surge-3}$ = 6.18 m, respectively. This is because as the entry angle increases, the contact area between the buoy and the wave surface decreases, which reduces the horizontal force exerted by the water surface on the buoy, leading to a smaller surge amplitude. Through analysis of the heave motion variation in Figure 21c under the three entry angles, it was observed that the buoy's heave angle amplitude is relatively small, less than 1.1°. When the buoy enters the water at initial angles of $\theta_{initial}$ = 0° and $\theta_{initial}$ = 20°, the heave motion exhibits a periodic fluctuation pattern. Combining the pitch motion variation in Figures 21d and 22, the buoy's pitch motion under the three entry angles also shows periodicity. The corresponding pitch angle amplitudes for the three entry angles are $\theta_{Pitch-1}$ = 16.5°, $\theta_{Pitch-2}$ = 17.0°, and $\theta_{Pitch-3}$ = 11.3°. From the analysis of the vertical overload variations after the buoy enters the water at three different entry angles in Figure 21e, it is observed that as the entry angle increases, the vertical overload gradually decreases. The maximum vertical overloads are a_{va-1} = 117.22 g, a_{va-2} = 95.56 g, and a_{va-3} = 78.74 g, respectively (where g is the acceleration due to gravity). This reduction is due to the decrease in the contact area between the buoy and the water surface as the entry angle increases, which reduces the force exerted on the buoy by the wave surface, thereby lowering the vertical overload. At smaller entry angles (0°), the buoy has a larger contact area with the wave surface, resulting in stronger hydrodynamic forces and higher vertical overloads.



(**a**) $\theta_{initial}$ = 0°



(**b**) $\theta_{initial}$ = 10°



(**c**) $\theta_{initial}$ = 20°

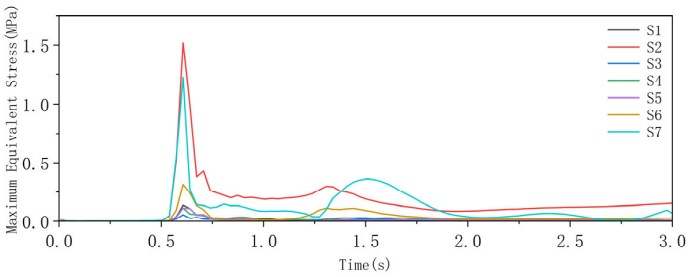
Figure 22. The motion attitude of the buoy under different entry angle conditions.

3.2. The Impact of Parametric Conditions on Buoy Water Entry Impact Loads

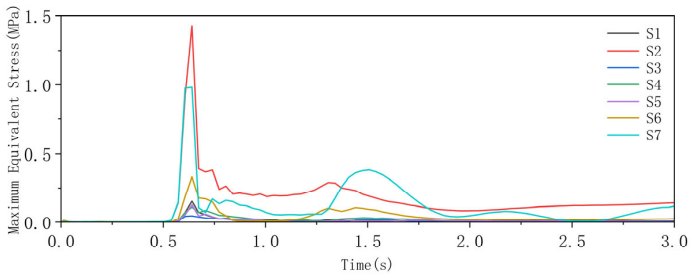
3.2.1. Wave Height

As shown in Figure 23, the stress variation curve at the external monitoring points of the buoy indicates that when the buoy is initially positioned at a height of $h_{initial}$ = 5 m above the horizontal plane with an initial angle $\theta_{initial}$ = 20°, and impacts waves with varying wave heights at a velocity of v_x = −1.82 m/s, v_y = 0 m/s v_z = −5 m/s, the stress increases sharply at the moment the buoy enters the water. Instantaneous peak stresses occur at t_1 = 0.61 s, t_2 = 0.64 s, and t_3 = 0.67 s; stress concentration is observed in the bottom S2 region and at the junction of the mast and the upper panel of the buoy, at S7.

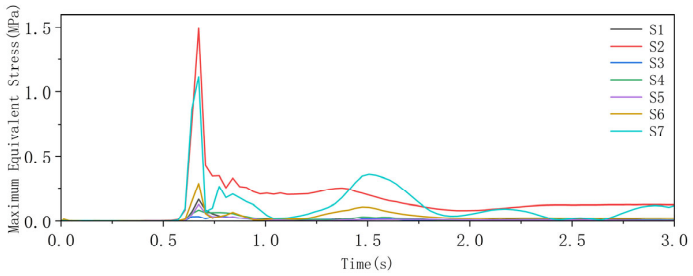
The maximum equivalent stress peak values reach F_{S2-h1} = 1.517 Mpa, F_{S7-h1} = 1.224 Mpa, F_{S2-h2} = 1.43 Mpa, F_{S7-h2} = 0.98 Mpa, F_{S2-h3} = 1.49 Mpa, and F_{S7-h3} = 1.12 Mpa. This phenomenon is primarily attributed to the viscosity and inertia of the water, which causes significant fluid resistance when the buoy enters the water, especially during the brief contact between the water surface and the buoy's surface. This creates immense pressure, resulting in a sharp increase in stress; the final result forms the maximum equivalent stress peak. Additionally, the S7 region, where the mast connects with the buoy's structure, is prone to stress concentration. Within t = 2~3 s, the variation in the maximum equivalent stress at all external monitoring points of the buoy is relatively small, with peak values remaining below 0.200 Mpa.



(**a**) h_1 = 0.5 m



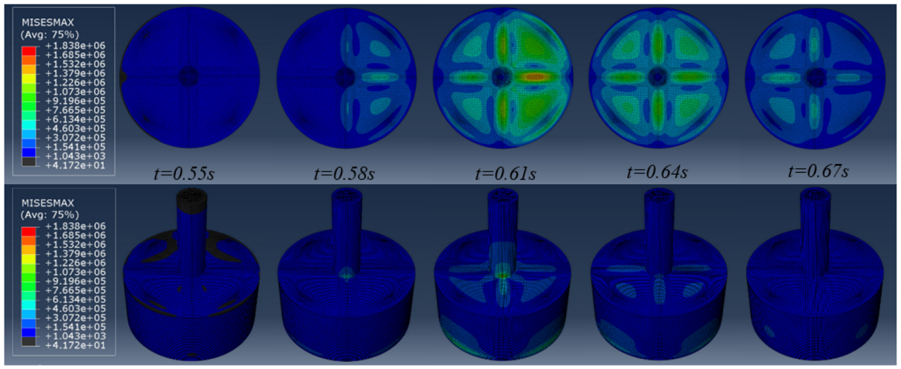
(**b**) h_2 = 1 m



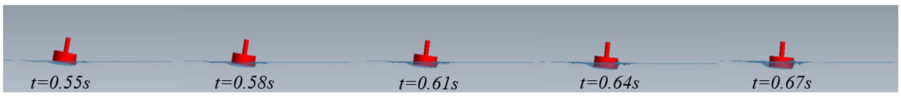
(**c**) h_3 = 2 m

Figure 23. Maximum equivalent stress variation curves at the external monitoring points of the buoy under different wave height conditions.

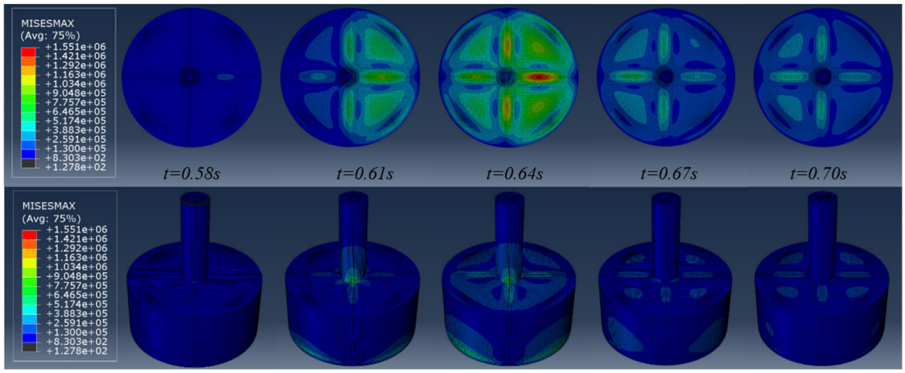
As shown in Figure 24, the stress contour map of the buoy's external monitoring points and the corresponding motion posture at each time moment, when the buoy impacts the water surface, reveals that the stress concentration area at the bottom of the buoy shifts from the right side to the left side. At the moment when the maximum equivalent stress peak is first reached, the stress concentration on the right side of the buoy's bottom is more prominent compared to the left side. Additionally, a distinct stress concentration is also observed in the S7 region of the buoy's upper panel. This phenomenon can be attributed to the uneven contact between the buoy's bottom and the flow field, with a larger contact area on the right side. As a result, the right side experiences a greater wave-induced force, leading to a more pronounced stress concentration in that area.



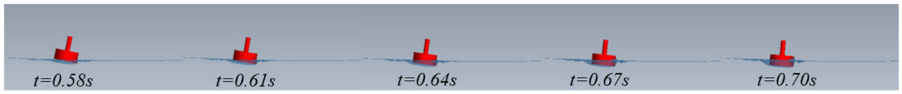
(**a**) Bottom and sides (h_1)



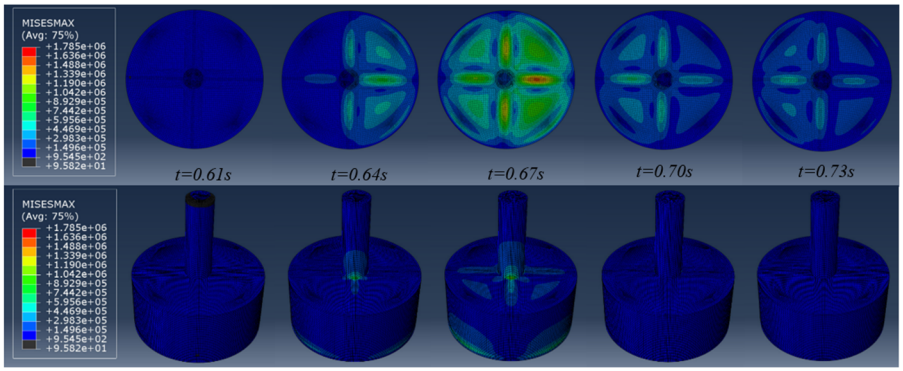
(**b**) Motion attitude at corresponding times (h_1)



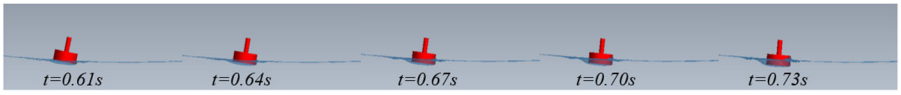
(**c**) Bottom and sides (h_2)



(**d**) Motion attitude at corresponding times (h_2)



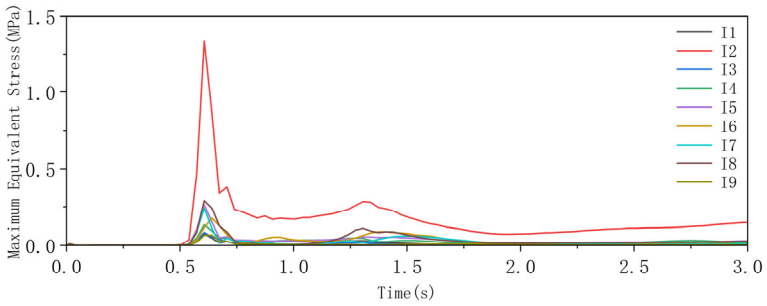
(**e**) Bottom and sides (h_3)



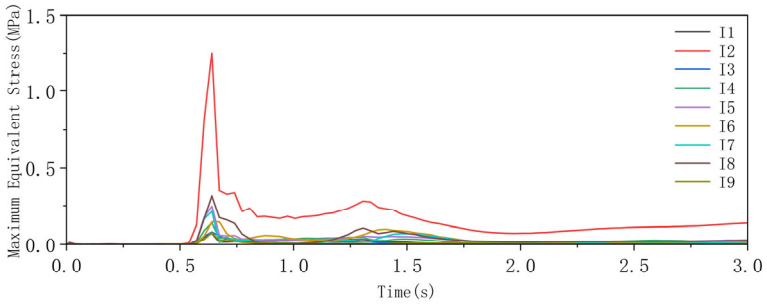
(**f**) Motion attitude at corresponding times (h_3)

Figure 24. The maximum equivalent stress clouds and corresponding motion attitudes of external monitoring points on the buoy under different wave height conditions (the clear legend of the maximum equivalent stress clouds can be found in Appendix A, as follows).

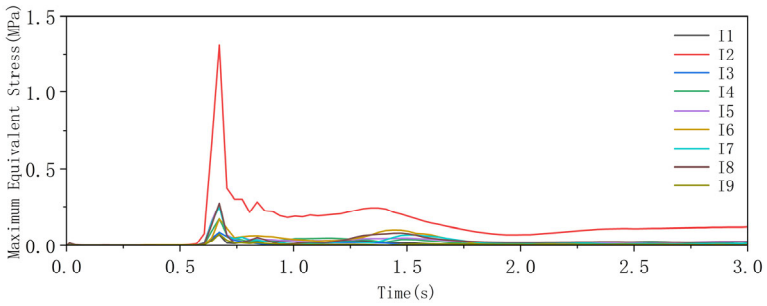
As shown in Figure 25, the stress variation curves of the buoy's cross-shaped plate monitoring points under different wave heights show that the buoy's cross-shaped plate experiences instantaneous peak values at t_1 = 0.61 s, t_2 = 0.64 s, and t_3 = 0.67 s, during which significant stress changes occur internally. The maximum equivalent stress peak at the I2 monitoring point reaches F_{I2-h1} = 1.34 Mpa, F_{I2-h2} = 1.25 Mpa, and F_{I2-h3} = 1.31 Mpa. The maximum equivalent stress peaks at other monitoring points on the buoy's cross-shaped plate are less than 0.3 Mpa. Within t = 2~3 s, the variation in the maximum equivalent stress at all monitoring points on the buoy's cross-shaped plate is relatively small.



(**a**) h_1 = 0.5 m



(**b**) h_2 = 1 m

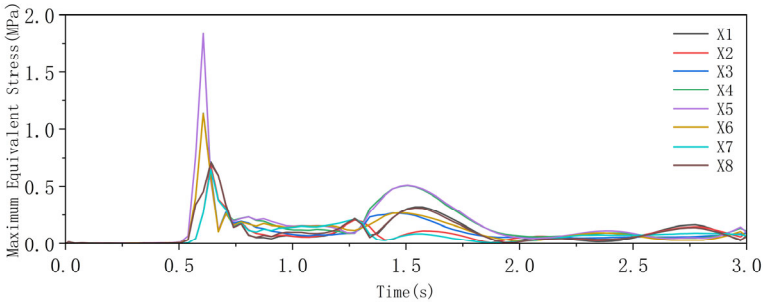


(**c**) h_3 = 2 m

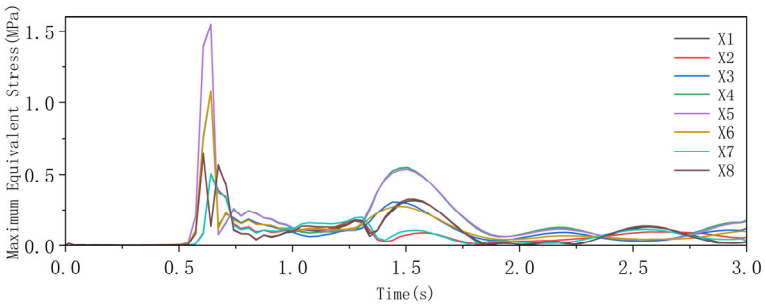
Figure 25. Maximum equivalent stress variation curves at the crossplate monitoring points of the buoy under different wave height conditions.

As shown in Figure 26, the stress variation curves of the monitoring points at the connection between the buoy's cross-shaped plate and the upper panel under different wave heights indicate that, due to the internal structural symmetry, the maximum equivalent stress values at X4 and X5 are equal. Under different wave heights, the monitoring points X4 and X5 at the connection between the cross-shaped plate and the top panel reach their maximum equivalent stress peak values at t_1 = 0.61 s, t_2 = 0.64 s, and t_3 = 0.67 s, with F_{X4-h1} = F_{X5-h1} = 1.84 MPa, F_{X4-h2} = F_{X5-h2} = 1.55 MPa, and F_{X4-h3} = F_{X5-h3} = 1.78 MPa. Within t = 2~3 s, the variation in the maximum equivalent stress at all monitoring points at the connection between the cross-shaped plate and the upper panel is relatively small, remaining below 0.25 MPa. The increased stress at the X4 and X5 regions can be attributed

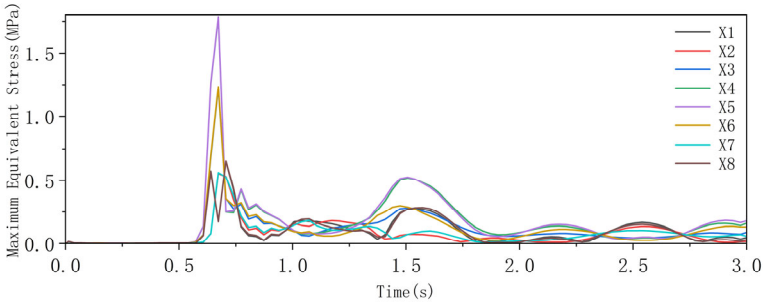
to the influence of water's inertia and viscosity during the buoy's tilted immersion. The shockwave generated upon immersion propagates along different directions on the water surface, forming varying hydrodynamic fields. The flow speed and wave-induced forces are higher on the right side, leading to greater stress in the areas corresponding to X4 and X5.



(**a**) h_1 = 0.5 m



(**b**) h_2 = 1 m

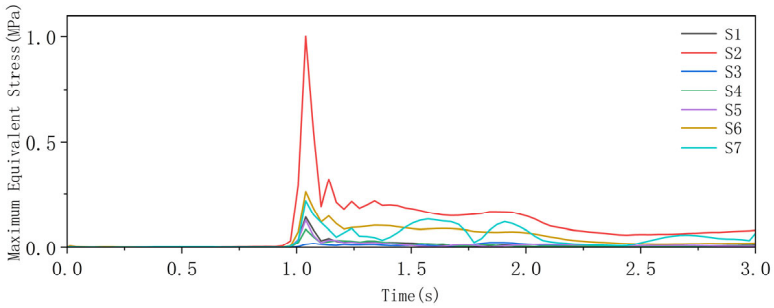


(**c**) h_3 = 2 m

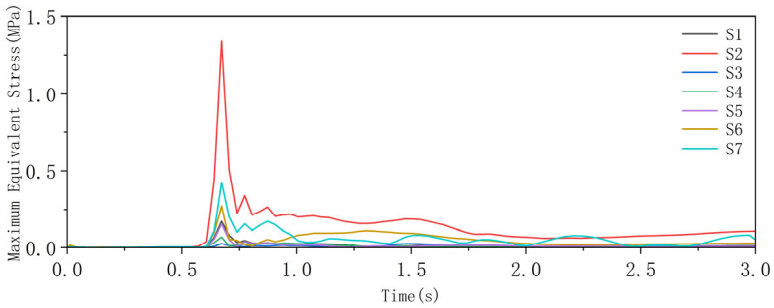
Figure 26. Maximum equivalent stress variation curves at the monitoring points of the connection between the crossplate and the upper panel of the buoy under different wave height conditions.

3.2.2. Entry Speed

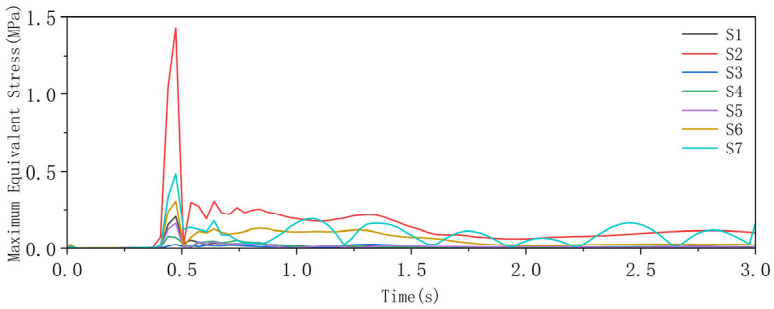
As shown in Figure 27, the stress variation curves of the external monitoring points on the buoy under different water entry velocities, with a wave height of h = 2 m, the buoy positioned at a distance of $h_{initial}$ = 5 m from the water surface and an initial tilt angle of $\theta_{initial} = 0°$, at impact wave velocities of v_v = 0 m/s, $v_v = -5$ m/s, $v_v = -10$ m/s, indicate a sharp increase in stress at the moment of water entry. Instantaneous peak stresses occur at t_1 = 1.04 s, t_2 = 0.67 s, t_3 = 0.47 s, with a stress concentration region observed at the bottom S2 area. The maximum equivalent stress peaks reach F_{S2-0} = 1.00 MPa, F_{S2-5} = 1.28 MPa, F_{S2-10} = 1.43 MPa, respectively. Within t = 2~3 s, the variation in the maximum equivalent stress at all external monitoring points on the buoy is small, with peak values below 0.25 MPa. As the buoy strikes the water surface at different speeds, the increase in water entry kinetic energy results in a corresponding increase in water resistance. The generated moment and fluid pressure due to the interaction between the wave and the buoy also increase, leading to a more concentrated stress distribution and higher peak values.



(**a**) v_v = 0 m/s



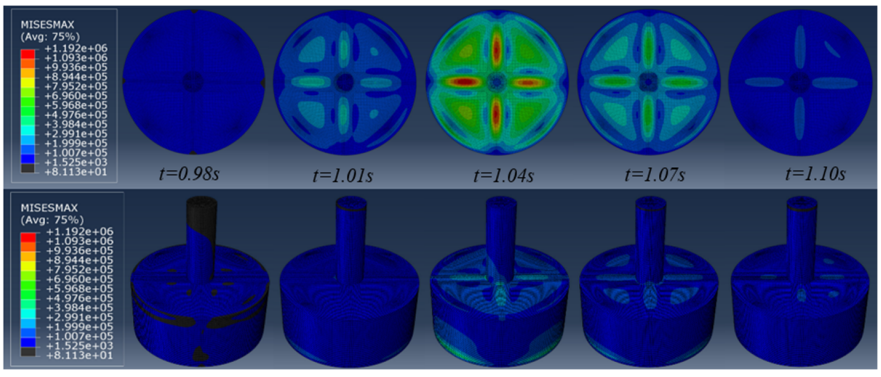
(**b**) v_v = −5 m/s



(**c**) v_v = −10 m/s

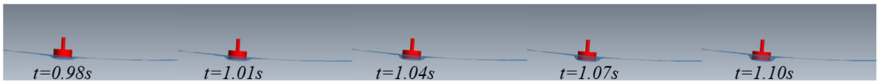
Figure 27. Maximum equivalent stress variation curves at the external monitoring points of the buoy under different entry speed conditions.

As shown in Figure 28, the stress contour plots of the external monitoring point areas and the corresponding motion postures of the buoy, when the buoy impacts the wave surface perpendicularly, reveal that the bottom of the buoy first contacts the water surface, and the contact with the wave surface is relatively uniform. Therefore, the water pressure distribution on the buoy's bottom is even, with the stress concentration area located in the bottom panel region exhibiting a certain degree of symmetry.

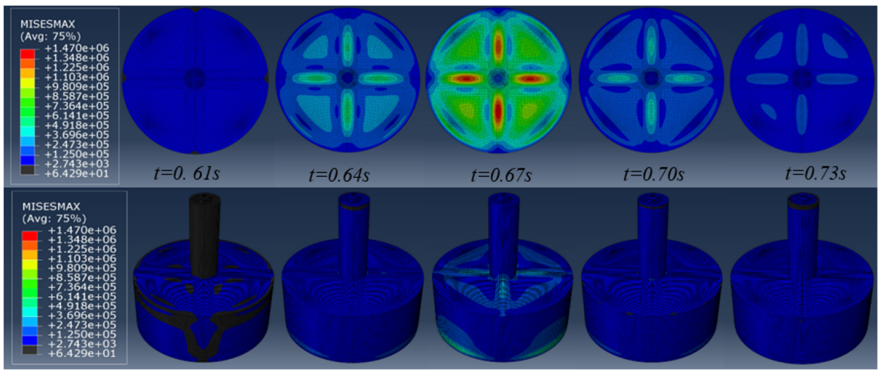


(**a**) Bottom and sides (v_v = 0 m/s)

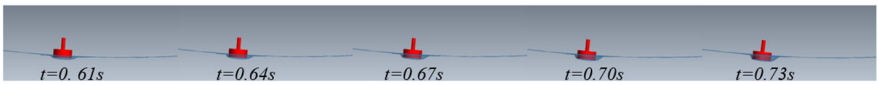
Figure 28. *Cont.*



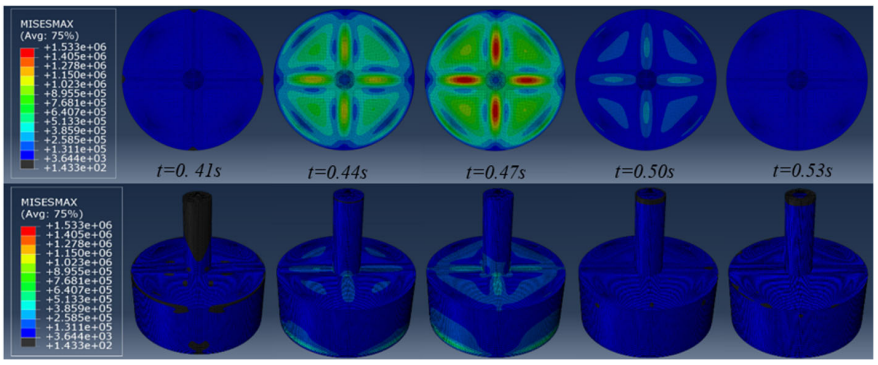
(**b**) Motion attitude at corresponding times (v_v = 0 m/s)



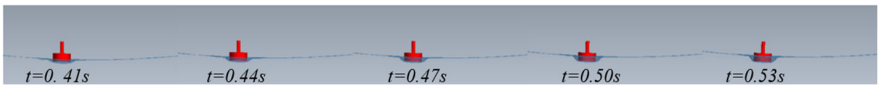
(**c**) Bottom and sides (v_v = −5 m/s)



(**d**) Motion attitude at corresponding times (v_v = −5 m/s)



(**e**) Bottom and sides (v_v = −10 m/s)



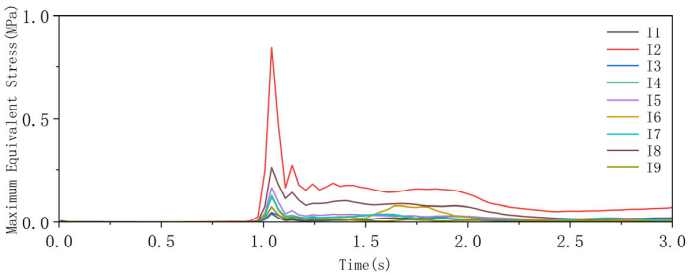
(**f**) Motion attitude at corresponding times (v_v = −10 m/s)

Figure 28. The maximum equivalent stress clouds and corresponding motion attitudes of external monitoring points on the buoy under different entry speed conditions.

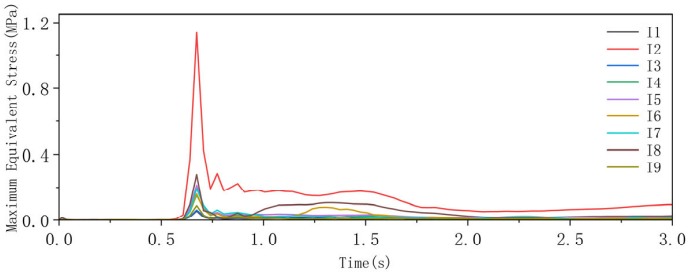
According to the stress variation curves of the cross-shaped plate monitoring points on the buoy under the different water entry velocities shown in Figure 29, the cross-shaped plate experiences instantaneous peak stresses at t_1 = 1.04 s, t_2 = 0.67 s, and t_3 = 0.47 s, with significant internal stress changes. The maximum equivalent stress peak at the I2 monitoring point reaches F_{I2-h1} = 0.85 Mpa, F_{I2-h2} = 1.09 Mpa, and F_{I2-h3} = 1.21 Mpa, while the maximum equivalent stress peaks at other monitoring points on the cross-shaped plate are all below 0.22 Mpa.

As shown in Figure 30, the stress variation curves of the monitoring points at the connection between the cross-shaped plate and the upper panel under different water entry velocities indicate that, due to the buoy's vertical water entry, the external surface experiences relatively uniform water pressure, and the symmetrical internal structure results in small differences in the maximum equivalent stress values across these monitoring points. Under different wave heights, the maximum equivalent stress peaks at the connection between the cross-shaped plate and the top panel occur at t_1 = 1.04 s, t_2 = 0.67 s, and t_3 = 0.47 s, with peak values ranging from 0.55 to 0.94 MPa, 0.92 to 1.05 MPa, and 1.03 to

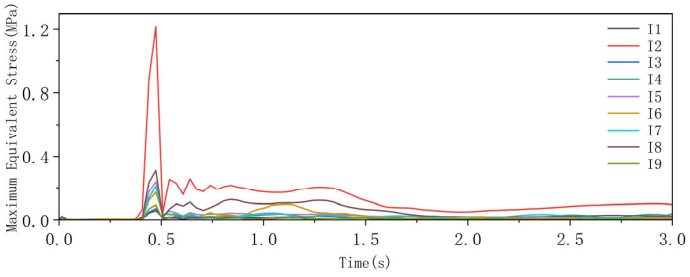
1.10 MPa, respectively. Within t = 2~3 s, the variation in the maximum equivalent stress at all monitoring points at the connection between the cross-shaped plate and the upper panel is small, remaining below 0.5 MPa.



(**a**) v_v= 0 m/s

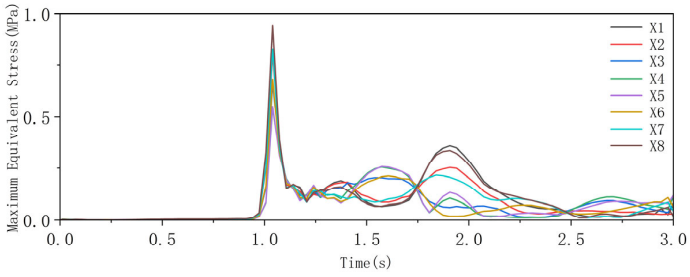


(**b**) v_v= −5 m/s

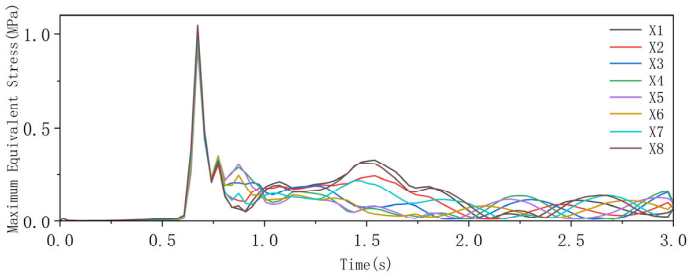


(**c**) v_v = −10 m/s

Figure 29. Maximum equivalent stress variation curves at the crossplate monitoring points of the buoy under different entry speed conditions.

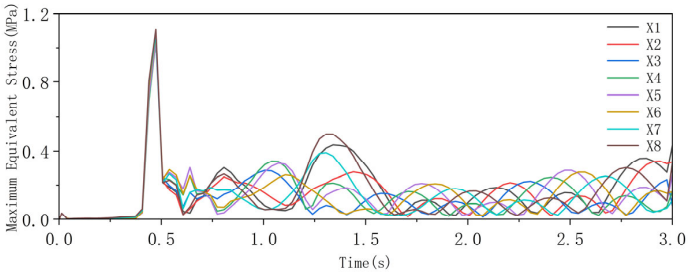


(**a**) v_v = 0 m/s



(**b**) v_v = −5 m/s

Figure 30. *Cont.*

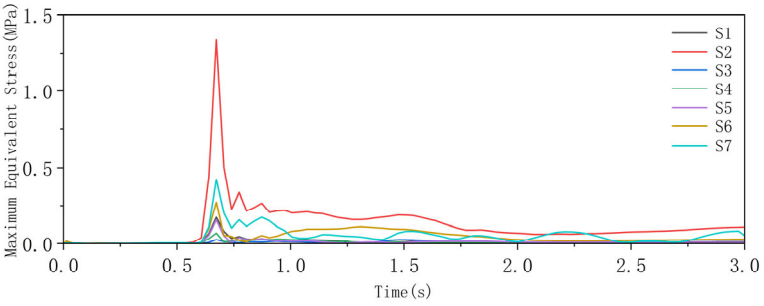


(**c**) v_v = −10 m/s

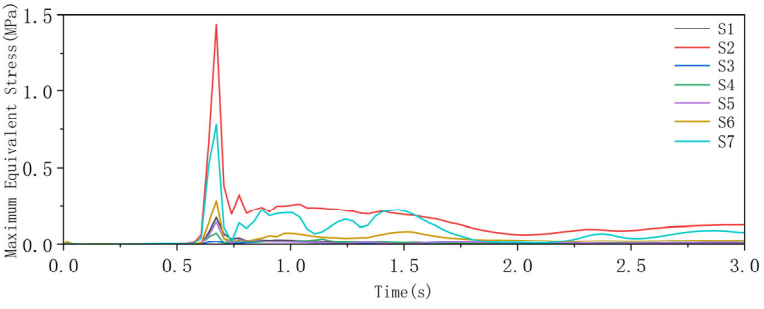
Figure 30. Maximum equivalent stress variation curves at the monitoring points of the connection between the crossplate and the upper panel of the buoy under different entry speed conditions.

3.2.3. Entry Angle

As shown in Figure 31, the stress variation curves at the external monitoring points on the buoy under different water entry angles, with the buoy at a distance of $h_{initial}$ = 5 m from the water surface, an initial velocity of $v_z = -5$ m/s, and entry angles of $\theta_{initial} = 0°$, 10°, and 20° impacting a wave surface with a wave height of h_3 = 2 m, indicate that the stress increases sharply at the moment of water entry, with instantaneous peak values occurring at t = 0.67 s. Stress concentration regions are observed at the bottom S2 area and the connection between the mast and the upper panel of the buoy at S7. The Maximum equivalent stress peaks reach $F_{S2-0°}$ = 1.28 MPa, $F_{S7-0°}$ = 0.35 MPa, $F_{S2-10°}$ = 1.44 MPa, $F_{S7-10°}$ = 0.78 MPa $F_{S2-20°}$ = 1.49 MPa, $F_{S7-20°}$ = 1.12 MPa, respectively. As the entry angle increases, the Maximum equivalent stress peaks at the S2 and S7 regions gradually increase. This phenomenon is due to the buoy's position near the wave trough, where larger entry angles reduce the contact area between the buoy's surface and the wave flow, causing uneven distribution of the wave's impact force. The force becomes concentrated primarily on the right side of the buoy's bottom, and the S2 and S7 regions, located on the right half of the buoy, lead to a gradual increase in the maximum equivalent stress peaks at the external monitoring points. Within t = 2~3 s, the maximum equivalent stress variation at all external monitoring points on the buoy remains small, with peak values below 0.200 MPa.

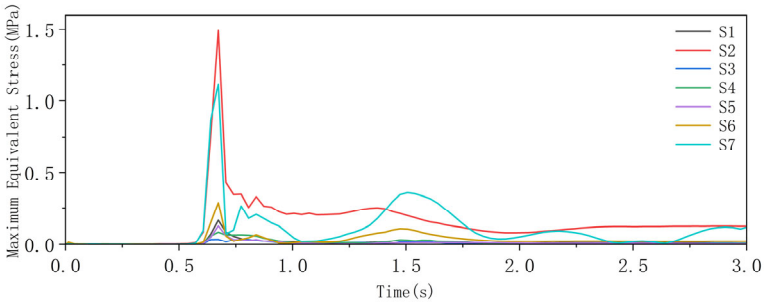


(**a**) $\theta_{initial}$ = 0°



(**b**) $\theta_{initial}$ = 10°

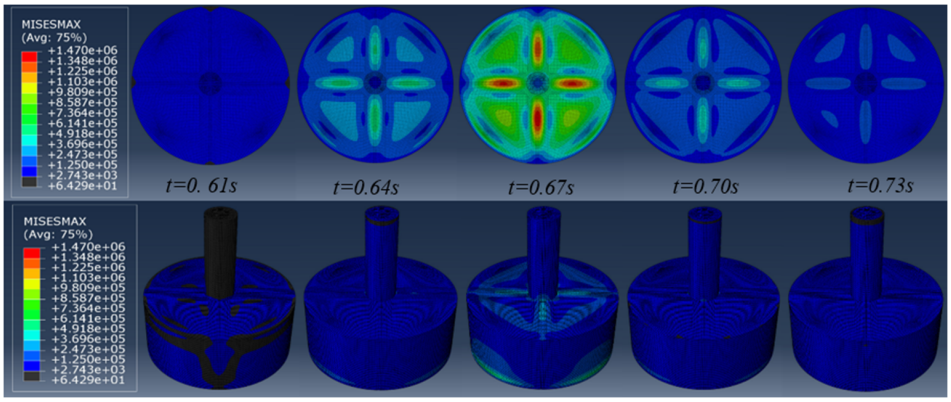
Figure 31. *Cont.*



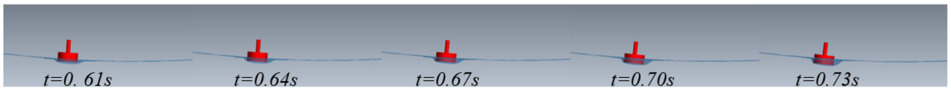
(**c**) $\theta_{initial}$ = 20°

Figure 31. The maximum equivalent stress variation curves at external monitoring points of the buoy under different entry angle conditions.

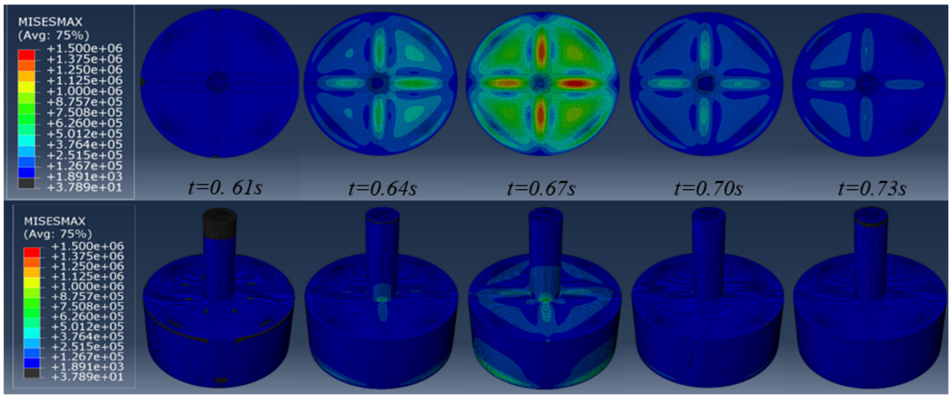
As shown in Figure 32, the stress contour plots at the external monitoring point regions and the corresponding motion postures of the buoy, when the buoy first reaches the maximum equivalent stress peak at the bottom, show that as the entry angle increases, the stress concentration region at the bottom shifts from a relatively uniform distribution to a noticeable offset toward the right side. The reason for this is that when the entry angle is small, the contact area between the buoy's bottom and the water surface is smaller, resulting in an uneven distribution of the wave's impact force. As the entry angle increases, the concentrated region of the wave's impact force shifts to the right side of the buoy, causing this offset phenomenon.



(**a**) Bottom and sides ($\theta_{initial}$ = 0°)

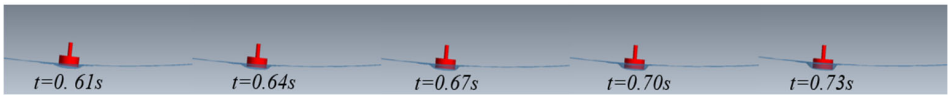


(**b**) Motion attitude at corresponding times ($\theta_{initial}$ = 0°)

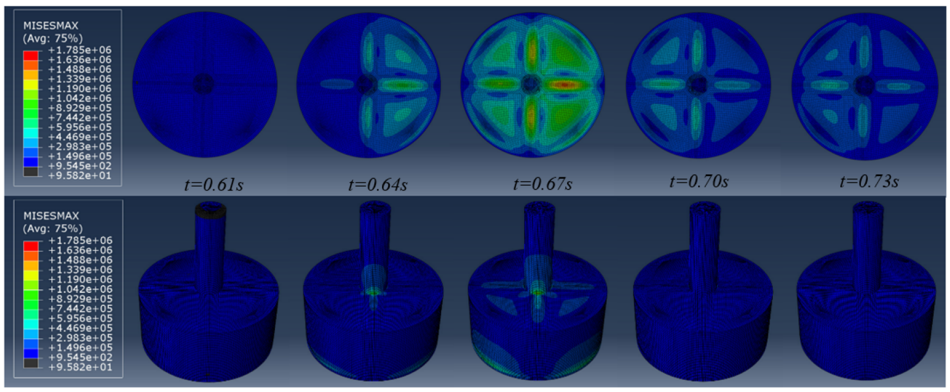


(**c**) Bottom and sides ($\theta_{initial}$ = 10°)

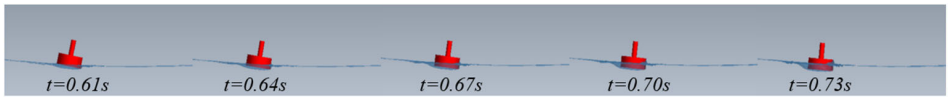
Figure 32. *Cont.*



(**d**) Motion attitude at corresponding times ($\theta_{initial}$ = 10°)



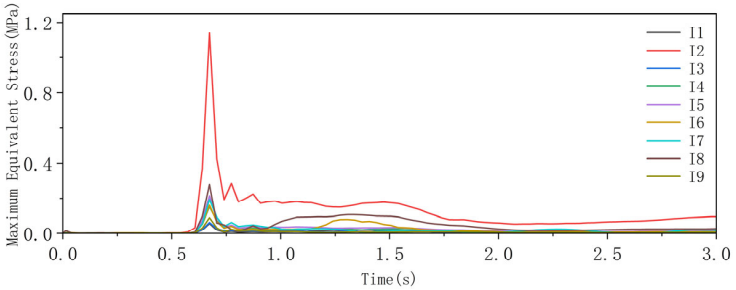
(**e**) Bottom and sides ($\theta_{initial}$ = 20°)



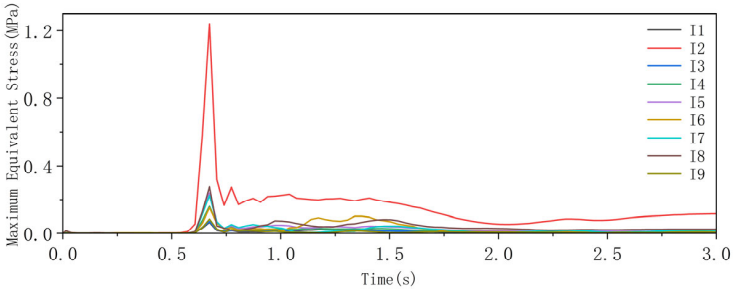
(**f**) Motion attitude at corresponding times ($\theta_{initial}$ = 20°)

Figure 32. The maximum equivalent stress clouds and corresponding motion attitudes of the external monitoring points on the buoy under different entry angle conditions.

According to Figure 33, the stress variation curves of the monitoring points on the buoy's cross-shaped plate under different water entry angles show that instantaneous peak stresses occur at t = 0.67 s, with significant internal stress variations. The maximum equivalent stress peak at the I2 monitoring point reaches F_{I2-0° = 1.09 MPa, F_{I2-10° = 1.24 MPa, and F_{I2-20° = 1.31 MPa, while the maximum equivalent stress peaks at other monitoring points on the cross-shaped plate are below 0.3 MPa. Within t = 2~3 s, the maximum equivalent stress variation at all monitoring points on the cross-shaped plate is small.

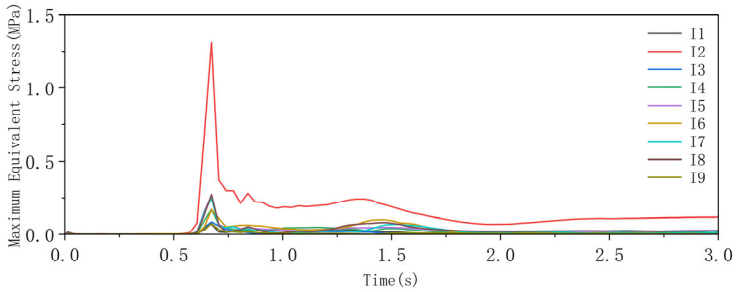


(**a**) $\theta_{initial}$= 0°



(**b**) $\theta_{initial}$ = 10°

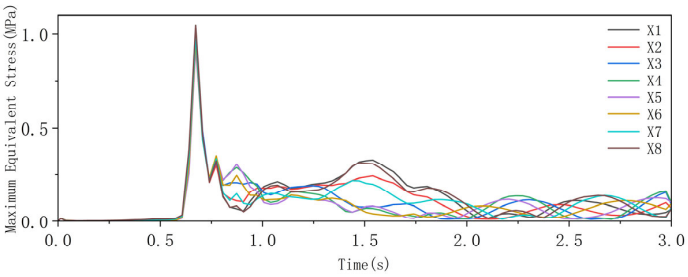
Figure 33. *Cont.*



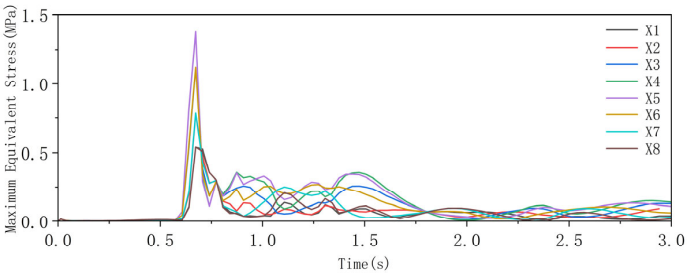
(**c**) $\theta_{initial}$ = 20°

Figure 33. The maximum equivalent stress variation curves at the crossplate monitoring points of the buoy under different entry angle conditions.

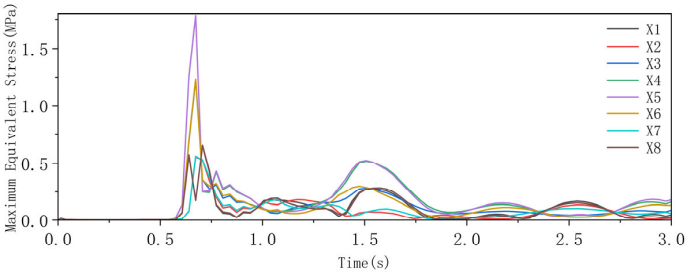
As shown in Figure 34, the stress variation curves at the monitoring points on the connection between the cross-shaped plate and the upper panel of the buoy under different water entry angles indicate that when $\theta_{initial}$ = 0°, the maximum equivalent stress peaks at the monitoring points on the connection between the cross-shaped plate and the upper panel show little difference, with peak values ranging from 0.82 MPa to 1.12 MPa. When $\theta_{initial}$ = 10° and 20°, due to the internal structural symmetry, the maximum equivalent stress values at the monitoring points are close to those at adjacent points, such as X4 and X5. When $\theta_{initial}$ = 10°, the first maximum equivalent stress peaks are $F_{X4-10°}$ = 1.37 MPa, and $F_{X5-10°}$ = 1.38 MPa. When $\theta_{initial}$ = 20°, the maximum equivalent stress peaks at both X4 and X5 are $F_{X4-20°} = F_{X5-20°}$ = 0.53 MPa.



(**a**) $\theta_{initial}$ = 0°



(**b**) $\theta_{initial}$ = 10°



(**c**) $\theta_{initial}$ = 20°

Figure 34. The maximum equivalent stress variation curves at the monitoring points of the connection between the crossplate and the upper panel of the buoy under different entry angle conditions.

3.3. Comprehensive Analysis of Impact Loads

In the parametric study of impact loads on the buoy discussed previously, at the external monitoring points S2 and S7, the crossplate monitoring point I2, and the connection points between the crossplate and the upper panel at X4 and X5 are areas where maximum equivalent stress concentrations occur. Therefore, a comprehensive analysis of these monitoring points was conducted.

As shown in Figure 35a, the analysis of the influence of wave height on the maximum equivalent stress peak indicates that changes in wave height affect the force state of the buoy in water, especially during wave impact. When the wave height increases, the buoy experiences stronger fluid pressure and dynamic effects at external monitoring points on the buoy surface (such as S7) and at the connection region between the cross-shaped plate and the upper panel (such as X4, X5). This is because the waves carry significant kinetic energy, and as the wave height increases, the water flow speed and impact force also increase, leading to higher stress at the buoy's surface and connection areas. The wave's impact force on the structure includes not only the dynamic pressure of the water flow but also the structural response vibrations. Especially under higher waves, the buoy's deformation and vibrations may amplify the local stresses in certain regions. From the analysis of the maximum equivalent stress peak variation with entry velocity in Figure 35b, it is clear that the entry velocity is a key factor influencing the buoy's water entry impact force. As the entry velocity increases, the relative speed between the buoy and the water body increases, resulting in a stronger impact force during water entry. In Figure 35b, the stress increments at monitoring points such as S2, S7, I2, X4, and X5 are relatively large. Higher entry velocities may result in stronger wave forces acting on the buoy's surface, and may even cause local water turbulence, further increasing the stress on structural components. From the analysis of the maximum equivalent stress peak variation with entry angle in Figure 35c, it is observed that as the entry angle increases, the contact area between the buoy's surface and the wave flow decreases. The distribution of the wave's impact force becomes uneven, primarily concentrating on the right side of the buoy's bottom. Since the S2 and S7 regions are located on the right half of the buoy, the stress at these monitoring points increases. Therefore, as the entry angle increases, the maximum equivalent stress peaks at S2, S7, I2, X4, and X5 gradually increase. Furthermore, the strength verification of the buoy reveals that the maximum equivalent stress peaks at all monitoring points are below the yield limit of the buoy material, which is 22 MPa (as shown in Table 3), indicating that the structural strength of the buoy remains within a safe range under all current water entry conditions.

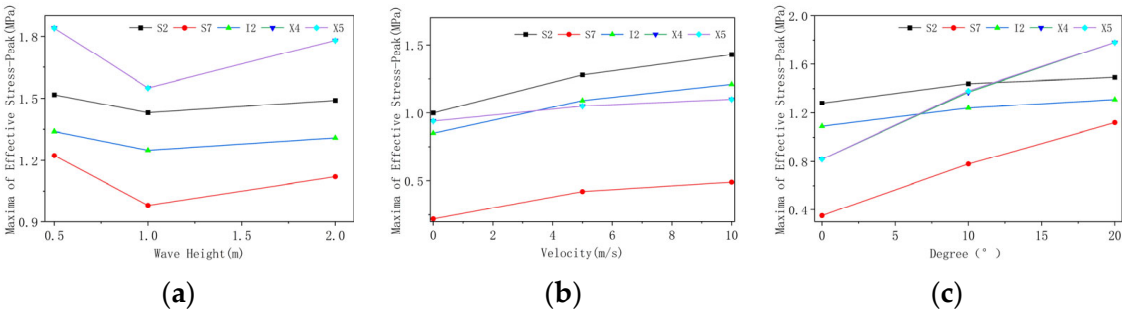


Figure 35. The impact of wave height, entry speed, and entry angle on the maximum equivalent stress peaks. (**a**) Maximum equivalent stress peak—wave height(Line X4 and line X5 coincide); (**b**) Maximum equivalent stress peak—speed; (**c**) Maximum equivalent stress peak—angle.

4. Conclusions

This paper utilized CFD numerical simulation methods to study the effects of wave height, entry speed, and entry angle on the water entry motion characteristics of heave, surge, roll, pitch, and vertical overload of a buoy under combined wave–current conditions. Additionally, through combined CFD and CAE simulation methods, the impact of wave height, entry speed, and entry angle on the impact loads of the external and internal components of the buoy after water entry was investigated, yielding the following main research results:

(1) Under the condition of maintaining the same flow velocity for different wave heights, as the wave height increases, the vertical distance between the buoy's water entry position and its initial position also increases. The buoy gains greater impact kinetic energy. Therefore, the maximum water entry depth of the buoy increases with wave height, resulting in a greater upward buoyancy force and a larger heaving amplitude. Since the buoy is primarily subjected to wave impact forces along the positive X-axis direction and the symmetry of its own structure along the Y-axis, the rolling amplitude is relatively smaller than the pitching amplitude. Under higher wave heights, the buoy's longitudinal resistance increases, causing the buoy's longitudinal motion to gradually stabilize. As a result, the pitching amplitude decreases with the increase in wave height. Under the same wave conditions, the trends of fluid resistance and the buoy's inertial response show similar patterns, so the entry velocity has a minor effect on the overall motion characteristics of the buoy after vertical water entry. A comparative analysis of the vertical overload peak values under different parameter conditions reveals that under different entry velocity conditions, the buoy has smaller vertical overload peaks when falling without initial velocity. When the buoy has an initial entry velocity, the corresponding vertical overload peak value is larger. This is because a higher entry velocity causes the buoy to contact the wave surface for a shorter period, resulting in a stronger reaction force from the water, which leads to a larger vertical overload. The entry angle is the main factor influencing the vertical overload peak. When the entry angle increases, the increment of the vertical overload peak decreases. This is because as the entry angle increases, the contact area between the buoy and the water surface decreases, leading to a reduction in the force acting on the buoy by the wave surface, thereby decreasing the vertical overload.

(2) Due to the viscosity and inertia of water, the buoy experiences significant fluid resistance at the moment of water entry, especially during the short period when the water surface and the buoy's surface are in contact. This results in a large pressure peak and a rapid increase in stress, forming instantaneous stress peaks at the buoy's internal component connections and external regions, thus creating stress concentration areas. Under different wave heights, when the buoy impacts the wave surface at an initial angle of $\theta_{initial}$= 20°, the buoy enters the water at an angle. Due to the uneven contact between the buoy's bottom and the flow field, the right side of the buoy's bottom contacts the wave surface first. Therefore, the right side of the buoy's bottom has a significant stress concentration area at the moment of water entry. Subsequently, the torque generated by the right side of the buoy causes the buoy to rotate around the Y-axis, resulting in water pressure on the left side of the buoy's bottom. The stress concentration area in the bottom region shifts from the right side to the left side. Since S7 is a structural connection point, there is a clear stress concentration region at the upper panel monitoring point S7. Under different velocity conditions, when the buoy impacts the wave surface vertically, the stress concentration region appears in the bottom panel area with some symmetry. As the entry kinetic energy increases, the fluid resistance also increases. The torque and fluid pressure generated by the

contact between the wave flow and the buoy will increase, leading to an increase in the structural stress of the buoy. Under different entry angle conditions, when the maximum equivalent stress peak is first reached at the bottom, with the increase in the entry angle, the stress concentration region at the bottom shifts from being relatively evenly distributed to being clearly to the right side. This is because the buoy enters the water near the wave trough, and a larger entry angle reduces the contact area between the buoy surface and the wave flow. The distribution of the impact force from the wave flow becomes uneven, concentrating on the right side of the buoy's bottom.

(3) After a comprehensive analysis of the impact load on the buoy's main monitoring points, it is found that changes in wave height have a significant impact on the stress peak values of the buoy's local regions, such as the external monitoring point S2 and the connection region between the cross-shaped plate and the upper panel (S7). With an increase in entry velocity and entry angle, stress increments are also significant at S2, S7, I2, X4, and X5. Comprehensive analysis reveals that entry velocity and entry angle are the primary factors affecting the water entry impact load on the buoy under wave flow conditions.

The limitations of the bidirectional fluid–structure interaction (FSI) method mainly lie in the following aspects: First, the interaction model between the fluid and the structure often assumes linear coupling, whereas in reality, the nonlinear behavior of both the fluid and the structure can introduce errors. Second, the computational resource requirements are substantial, especially when dealing with complex geometries and large-scale simulations, leading to high computational costs. In response to the current limitations in research, future studies may focus on the development of more accurate nonlinear coupling models, particularly in the context of large deformations, strong nonlinear fluid behavior, or complex materials. Considering nonlinear coupling will contribute to improving the accuracy and reliability of simulation results. Additionally, the development of novel solvers and new adaptive mesh methods could reduce computational costs and enhance the efficiency of solving large-scale fluid–structure interaction problems, which may also become a key focus in future research.

Author Contributions: W.G.: conceptualization, methodology, validation, software, and writing—original draft. X.Y.: validation, software, investigation, and writing—review and editing. H.C.: resources, project administration, and writing—review and editing. S.W.: funding acquisition and resources. J.Z.: funding acquisition, supervision, and resources. L.J.: funding acquisition and resources. H.L.: conceptualization and resources. All authors have read and agreed to the published version of the manuscript.

Funding: This study was supported by the National Natural Science Foundation of China (52071095); the National Key R&D Program of China (Grant No. 2022YFB4200705); Taishan Scholar Foundation of Shandong Province; Fundamental Research Funds for the Central Universities (3072024XX2715); Science Fund of Shandong Laboratory of Advanced Materials and Green Manufacturing (Yantai) (AMGM2023F02, AMGM2023F07), the program of KY10100230078 and B72E9B3A.

Institutional Review Board Statement: Not applicable.

Informed Consent Statement: Not applicable.

Data Availability Statement: Data are contained within the article.

Conflicts of Interest: Jian Zhang and Lixue Jiang were employed by the China Resources Gas Investment (China) Limited. The remaining authors declare that the research was conducted in the absence of any commercial or financial relationships that could be construed as a potential conflict of interest.

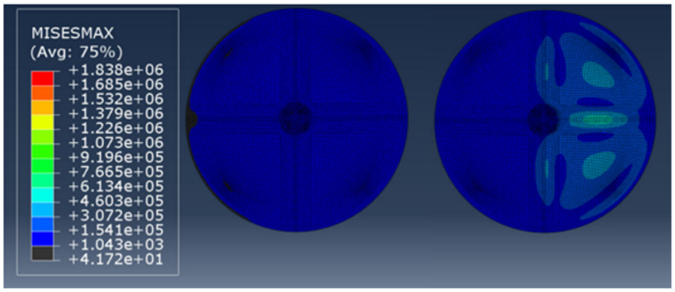
Nomenclature

The definitions of the terms related to this study are provided in the table below.

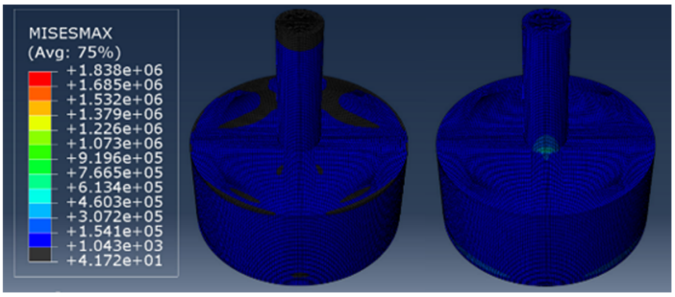
$\theta_{initial}$	Initial Entry Angle
$h_{initial}$	Initial Height
v_v	Initial Entry Speed
D	Buoy Diameter
h	Wave Height
v_f	Flow Speed
$h_{amplitude}$	Wave Amplitude
h_{max-n}	Maximum Submersion Depth
T_{Roll}	Roll Period
θ_{Roll}	Roll Amplitude
$\theta_{Pitch-n}$	Pitch Amplitude
a_{va-n}	Vertical Overload
$x_{Surge-n}$	Surge Distance
F_{Sn-n}	Maximum Equivalent Stress Peak

Appendix A

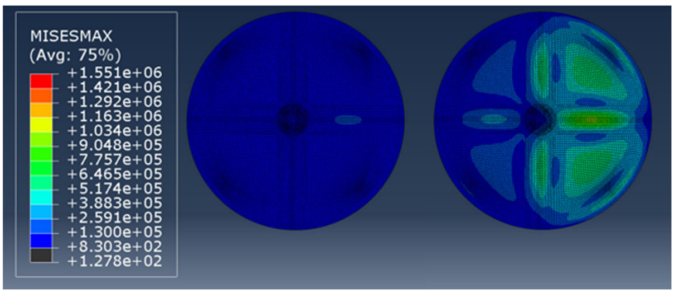
The following section provides supplementary stress contour plots of the buoy's external monitoring points under parametric conditions, along with the corresponding motion posture diagrams at specific moments. Due to space limitations in the main text, the legends in the stress contour plots were not clearly displayed. In this appendix, they have been enlarged for better clarity and to ensure the information in the images is clearly presented.



(**a**) Bottom t = 0.55 s and t = 0.58 s (h_1)

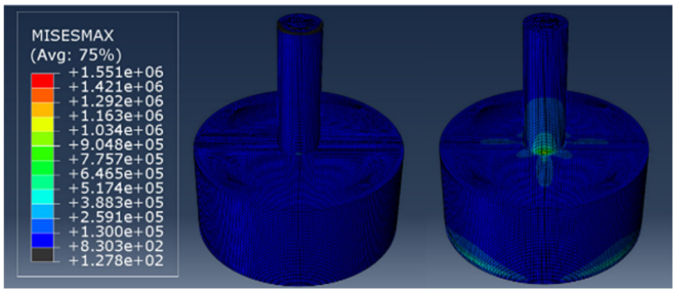


(**b**) Sides t = 0.55 s and t = 0.58 s (h_1)

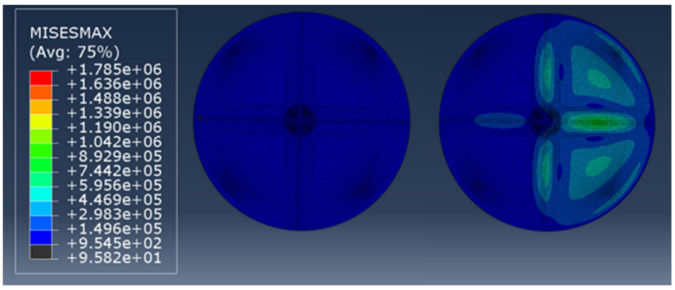


(**c**) Bottom t = 0.58 s and t = 0.61 s (h_2)

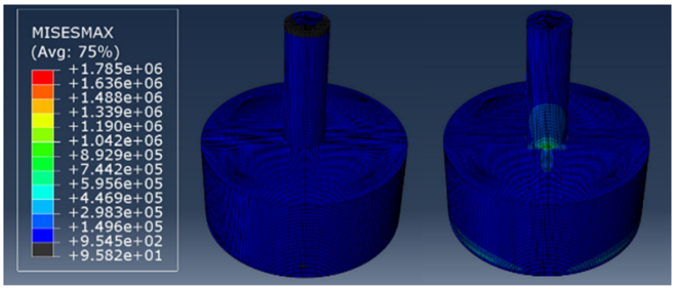
Figure A1. *Cont.*



(**d**) Sides t = 0.58 s and t = 0.61 s (h_2)

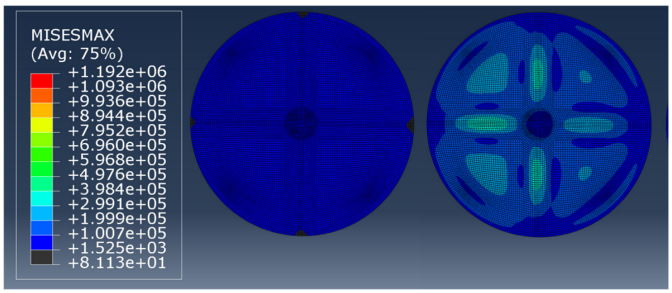


(**e**) Bottom t = 0.61 s and t = 0.64 s (h_3)

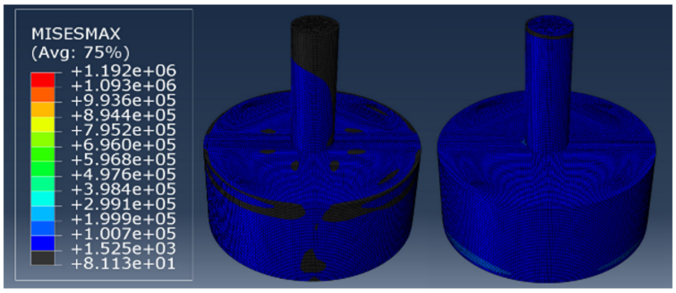


(**f**) Sides t = 0.61 s and t = 0.64 s (h_3)

Figure A1. Maximum equivalent stress clouds under different wave height conditions.

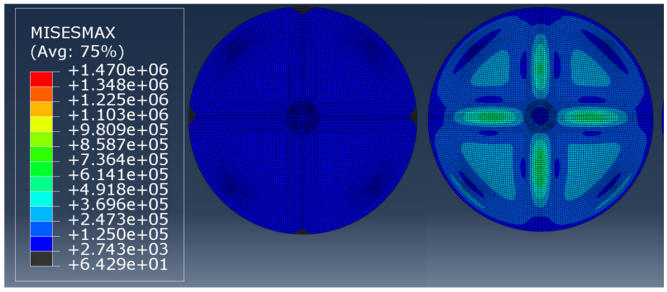


(**a**) Bottom t = 0.98 s and t = 1.01 s (v_v = 0 m/s)

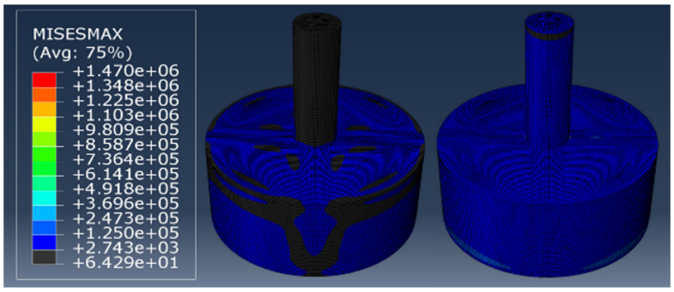


(**b**) Sides t = 0.98 s and t = 1.01 s (v_v = 0 m/s)

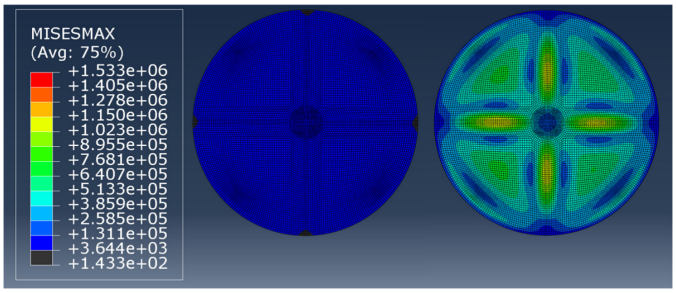
Figure A2. *Cont*.



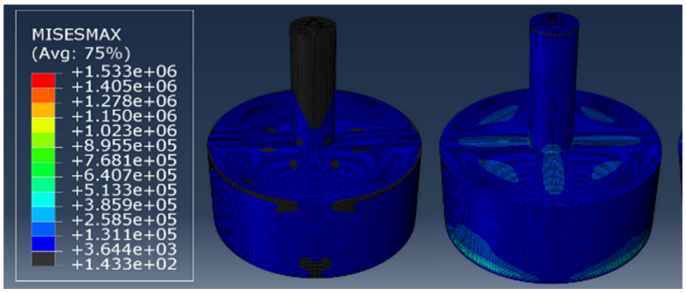
(**c**) Bottom t = 0.61 s and t = 0.64 s (v_v = −5 m/s)



(**d**) Sides t = 0.61 s and t = 0.64 s (v_v = −5 m/s)

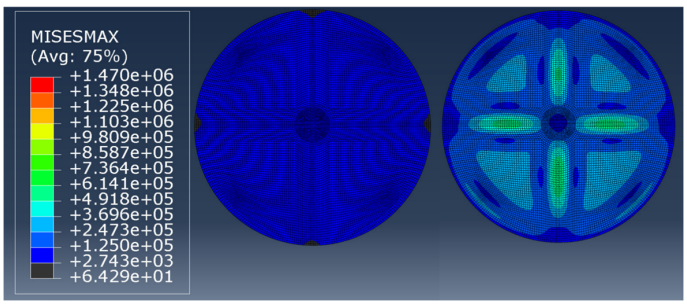


(**e**) Bottom t = 0.41 s and t = 0.44 s (v_v = −10 m/s)



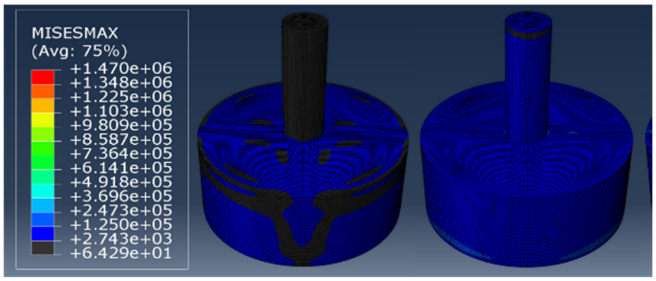
(**f**) Sides t = 0.41 s and t = 0.44 s (v_v = −10 m/s)

Figure A2. Maximum equivalent stress clouds under different entry speed conditions.

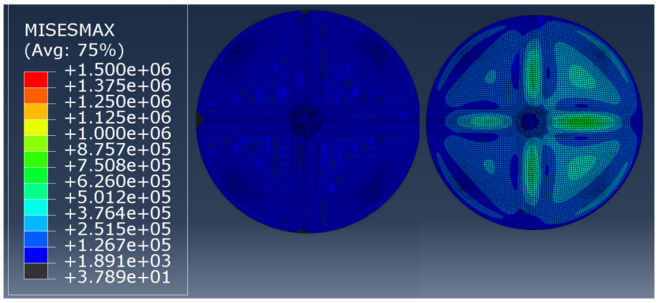


(**a**) Bottom t = 0.61 s and t = 0.64 s ($\theta_{initial}$ = 0°)

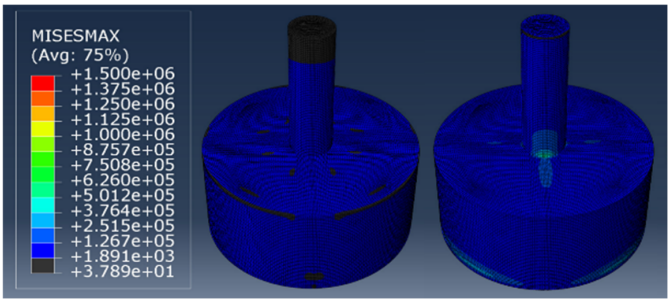
Figure A3. *Cont.*



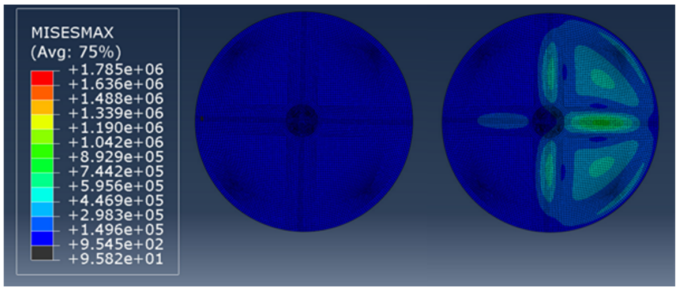
(**b**) Sides t = 0.61 s and t = 0.64 s ($\theta_{initial}$ = 0°)



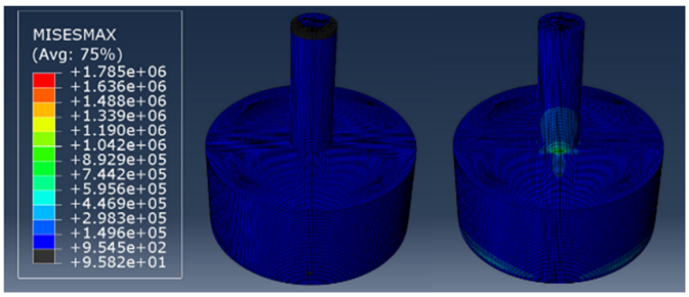
(**c**) Bottom t = 0.61 s and t = 0.64 s ($\theta_{initial}$ = 10°)



(**d**) Sides t = 0.61 s and t = 0.64 s ($\theta_{initial}$ = 10°)



(**e**) Bottom t = 0.61 s and t = 0.64 s ($\theta_{initial}$ = 20°)



(**f**) Sides t = 0.61 s and t = 0.64 s ($\theta_{initial}$ = 20°)

Figure A3. Maximum equivalent stress clouds under different entry angle conditions.

References

1. Majumder, A.; Losito, M.; Paramasivam, S.; Kumar, A.; Gatto, G. Buoys for marine weather data monitoring and LoRaWAN communication. *Ocean Eng.* **2024**, *313*, 119521. [CrossRef]
2. Wu, Y.; Bakker DC, E.; Achterberg, E.P.; Silva, A.N.; Pickup, D.D.; Li, X.; Hartman, S.; Stappard, D.; Qi, D.; Tyrrell, T. Integrated analysis of carbon dioxide and oxygen concentrations as a quality control of ocean float data. *Commun. Earth Environ.* **2022**, *3*, 92. [CrossRef]
3. Von Karman, T. *The Impact on Sea Plane Floats During Landing*; National Advisory Committee for Aeronautics: Washington, DC, USA, 1929.
4. Wagner, H. The phenomena of impact and planing on water. *Natl. Advis. Comm. Aeronaut. Transl. 1366 ZAMM* **1932**, *12*, 193–215.
5. Dobrovol'Skaya, Z.N. On some problems of similarity flow of fluid with a free surface. *J. Fluid Mech.* **1969**, *36*, 805–829. [CrossRef]
6. Greenhow, M. Wedge entry into initially calm water. *Appl. Ocean Res.* **1987**, *9*, 214–223. [CrossRef]
7. Zhao, R.; Faltinsen, O. Water entry of two-dimensional bodies. *J. Fluid Mech.* **1993**, *246*, 593–612. [CrossRef]
8. Zhao, R. Water entry of arbitrary two-dimensional sections with and without flow separation. In Proceedings of the 21st Symposium on Naval Hysdrodynamics, Trondheim, Norway, 18–20 May 2011; National Academy Press: Washington, DC, USA, 1996; pp. 408–423.
9. Korobkin, A. Blunt-body impact on a compressible liquid surface. *J. Fluid Mech.* **1992**, *244*, 437–453. [CrossRef]
10. Fraenkel, L.E.; McLeod, J.B. Some results for the entry of a blunt wedge into water. Philosophical Transactions of the Royal Society of London. *Ser. A Math. Phys. Eng. Sci.* **1997**, *355*, 523–535. [CrossRef]
11. Scolan, Y.M.; Korobkin, A.A. Energy distribution from vertical impact of a three-dimensional solid body onto the flat free surface of an ideal fluid. *J. Fluids Struct.* **2003**, *17*, 275–286. [CrossRef]
12. Lauria, A.; Loprieno, P.; Rizzo, F.; Severini, A.; Foti, D.; Leone, E.; Francone, A.; Tomasicchio, G. On the effects of wind and operating conditions on mooring line tensions for floating offshore wind turbine. *Appl. Ocean Res.* **2024**, *152*, 104197. [CrossRef]
13. Mohapatra, S.C.; Amouzadrad, P.; Baldaconi da Silva Bispo, I.; Soares, C.G. Hydrodynamic Response to Current and Wind on a Large Floating Interconnected Structure. *J. Mar. Sci. Eng.* **2025**, *13*, 63. [CrossRef]
14. Wu, S.Q.; Kang, X.W. Research on hydro-dynamic of Column Body water-entry with six-DOF at high-speed. *Appl. Mech. Mater.* **2014**, *533*, 40–43. [CrossRef]
15. Qi, D.; Feng, J.; Xu, B.; Zhang, J.; Li, Y. Investigation of water entry impact forces on airborne-launched AUVs. *Eng. Appl. Comput. Fluid Mech.* **2016**, *10*, 473–484. [CrossRef]
16. Wang, X.; Shi, Y.; Pan, G.; Chen, X.; Zhao, H. Numerical research on the high-speed water entry trajectories of AUVs with asymmetric nose shapes. *Ocean Eng.* **2021**, *234*, 109274. [CrossRef]
17. Hu, X.; Liu, S. Numerical investigation of water-entry of flatted-bottom seafloor mining tool in ocean waves. *J. Cent. South Univ.* **2014**, *21*, 3071–3078. [CrossRef]
18. Takami, T.; Matsui, S.; Oka, M.; Iijima, K. A numerical simulation method for predicting global and local hydroelastic response of a ship based on CFD and FEA coupling. *Mar. Struct.* **2018**, *59*, 368–386. [CrossRef]
19. Li, Z.; Hu, H.; Wang, C.; Xie, Z.; Chen, X.; Yuan, Z.; Du, P. Hydrodynamics and stability of oblique water entry in waves. *Ocean Eng.* **2024**, *292*, 116506. [CrossRef]
20. Zhang, G.; Hou, Z.; Sun, T.; Wei, H.; Li, N.; Zhou, B.; Gao, Y. Numerical simulation of the effect of waves on cavity dynamics for oblique water entry of a cylinder. *J. Hydrodyn.* **2020**, *32*, 1178–1190. [CrossRef]
21. Tregde, V. Compressible air effects in CFD simulations of free fall lifeboat drop. In Proceedings of the International Conference on Offshore Mechanics and Arctic Engineering, St. John's, NL, Canada, 31 May–5 June 2015; American Society of Mechanical Engineers: New York, NY, USA, 2015; Volume 56482, p. V002T08A018.
22. Huang, L.; Tavakoli, S.; Li, M.; Dolatshah, A.; Pena, B.; Ding, B.; Dashtimanesh, A. CFD analyses on the water entry process of a freefall lifeboat. *Ocean Eng.* **2021**, *232*, 109115. [CrossRef]
23. Sauder, T.; Croonenborghs, E.; Fouques, S.; Berchiche, N.; Reinholdtsen, S.A. Effect of wind loads on the performance of free-fall lifeboats. In Proceedings of the International Conference on Offshore Mechanics and Arctic Engineering, San Francisco, CA, USA, 8–13 June 2014; American Society of Mechanical Engineers: New York, NY, USA, 2014; Volume 45431, p. V04BT02A033.
24. Torheim, S.; Gudmestad, O.T. Secure launch of lifeboats in cold climate: Looking into requirements for winterization. In Proceedings of the International Conference on Offshore Mechanics and Arctic Engineering, Rotterdam, The Netherlands, 19–24 June 2011; Volume 44335, pp. 931–939.
25. Ré AJ, S.; Veitch, B. Evacuation in ice: Ice loads on a lifeboat during field trials. In Proceedings of the International Conference on Offshore Mechanics and Arctic Engineering, Nantes, France, 9–14 June 2013; American Society of Mechanical Engineers: New York, NY, USA, 2013; Volume 55409, p. V006T07A015.
26. Breton, T.; Tassin, A.; Jacques, N. Experimental investigation of the water entry and/or exit of axisymmetric bodies. *J. Fluid Mech.* **2020**, *901*, A37. [CrossRef]

27. Wei, Z.; Hu, C. Experimental study on water entry of circular cylinders with inclined angles. *J. Mar. Sci. Technol.* **2015**, *20*, 722–738. [CrossRef]
28. De Backer, G.; Vantorre, M.; Beels, C.; De Pré, J.; Victor, S.; De Rouck, J.; Blommaert, C.; Van Paepegem, W. Experimental investigation of water impact on axisymmetric bodies. *Appl. Ocean Res.* **2009**, *31*, 143–156. [CrossRef]
29. Shams, A.; Jalalisendi, M.; Porfiri, M. Experiments on the water entry of asymmetric wedges using particle image velocimetry. *Phys. Fluids* **2015**, *27*, 027103. [CrossRef]
30. Sun, L.; Wang, D.; Chen, Y.; Wu, G. Numerical and experimental investigation on the oblique water entry of cylinder. *Sci. Prog.* **2020**, *103*, 0036850420940889. [CrossRef]
31. Yan, G.X.; Pan, G.; Shi, Y.; Wang, G. Experimental study on water entry of cylindrical projectiles with different nose shapes. *Mod. Phys. Lett. B* **2019**, *33*, 1950107. [CrossRef]
32. Truscott, T.T.; Techet, A.H. A spin on cavity formation during water entry of hydrophobic and hydrophilic spheres. *Phys. Fluids* **2009**, *21*, 121703. [CrossRef]
33. Hurd, R.C.; Belden, J.; Jandron, M.A.; Fanning, D.T.; Bower, A.F.; Truscott, T.T. Water entry of deformable spheres. *J. Fluid Mech.* **2017**, *824*, 912–930. [CrossRef]
34. Li, D.; Zhang, J.; Zhang, M.; Huang, B.; Ma, X.; Wang, G. Experimental study on water entry of spheres with different surface wettability. *Ocean Eng.* **2019**, *187*, 106123. [CrossRef]
35. Panciroli, R.; Ubertini, S.; Minak, G.; Jannelli, E. Experiments on the dynamics of flexible cylindrical shells impacting on a water surface. *Exp. Mech.* **2015**, *55*, 1537–1550. [CrossRef]
36. Ren, Z.; Wang, Z.; Stern, F.; Judge, C.; Ikeda-Gilbert, C. Vertical water entry of a flexible wedge into calm water: A fluid-structure interaction experiment. *J. Ship Res.* **2019**, *63*, 41–55. [CrossRef]
37. Gilbarg, D.; Anderson, R.A. Influence of atmospheric pressure on the phenomena accompanying the entry of spheres into water. *J. Appl. Phys.* **1948**, *19*, 127–139. [CrossRef]
38. May, A. Effect of surface condition of a sphere on its water-entry cavity. *J. Appl. Phys.* **1951**, *22*, 1219–1222. [CrossRef]
39. May, A. *Water Entry and the Cavity-Running Behavior of Missiles*; NAVSEA Hydrodynamics Advisory Committee: Silver Spring, MD, USA, 1975.
40. Aristoff, J.M.; Bush, J.W.M. Water entry of small hydrophobic spheres. *J. Fluid Mech.* **2009**, *619*, 45–78. [CrossRef]
41. Panciroli, R.; Falcucci, G.; Erme, G.; De Santis, E.; Jannelli, E. Fluid-structure interaction during the water entry of flexible cylinders. *AIP Conf. Proc.* **2015**, *1648*, 570011.
42. Guo, Z.; Zhang, W.; Xiao, X.; Wei, G.; Ren, P. An investigation into horizontal water entry behaviors of projectiles with different nose shapes. *Int. J. Impact Eng.* **2012**, *49*, 43–60. [CrossRef]
43. Guo, Z.; Zhang, W.; Wang, C. Experimental and theoretical study on the high-speed horizontal water entry behaviors of cylindrical projectiles. *J. Hydrodyn.* **2012**, *24*, 217–225. [CrossRef]
44. Shi, H.H.; Itoh, M.; Takami, T. Optical observation of the supercavitation induced by high-speed water entry. *J. Fluids Eng.* **2000**, *122*, 806–810. [CrossRef]
45. Truscott, T.T.; Techet, A.H. Water entry of spinning spheres. *J. Fluid Mech.* **2009**, *625*, 135–165. [CrossRef]
46. Hou, Z.; Sun, T.; Quan, X.; Zhang, G.; Sun, Z.; Zong, Z. Large eddy simulation and experimental investigation on the cavity dynamics and vortex evolution for oblique water entry of a cylinder. *Appl. Ocean Res.* **2018**, *81*, 76–92. [CrossRef]
47. Li, S.B.; Ming, F.R.; Peng, T.S.; Sui, Y. Experimental study on the elastic response characteristics of a rotating body under an oblique water impact load. *Ocean Eng.* **2024**, *310*, 118643. [CrossRef]

Disclaimer/Publisher's Note: The statements, opinions and data contained in all publications are solely those of the individual author(s) and contributor(s) and not of MDPI and/or the editor(s). MDPI and/or the editor(s) disclaim responsibility for any injury to people or property resulting from any ideas, methods, instructions or products referred to in the content.